Development of photoactivatable CO-releasing tricarbonylrhenium(I) complexes and their integration into cellulose nanocrystals in view of antibacterial activity

Valentine Guilbaud, Marie Goizet, Nadine Leygue, Alexandre Poirot, Sonia Mallet-Ladeira, Charles-Louis Serpentini, Tan-Sothéa Ouk, Gauthier M A Ndong Ntoutoume, Vincent Sol, Eric Benoist, et al.

Journal of Photochemistry & Photobiology, A: Chemistry 453 (2024) 115600

Contents lists available at ScienceDirect

Journal of Photochemistry & Photobiology, A: Chemistry

journal homepage: www.elsevier.com/locate/jphotochem

Development of photoactivatable CO-releasing tricarbonylrhenium(I) complexes and their integration into cellulose nanocrystals in view of antibacterial activity

Valentine Guilbaud [a], Marie Goizet [a], Nadine Leygue [a], Alexandre Poirot [a], Sonia Mallet-Ladeira [b], Charles-Louis Serpentini [c], Tan-Sothéa Ouk [d], Gauthier M.A. Ndong Ntoutoume [d], Vincent Sol [d], Eric Benoist [a], Suzanne Fery-Forgues [a,*]

[a] SPCMIB, CNRS UMR 5068, Université de Toulouse III Paul Sabatier, 118 route de Narbonne, 31062 Toulouse cedex 9, France
[b] Service Diffraction des Rayons X, Institut de Chimie de Toulouse, ICT- UAR 2599, Université de Toulouse III Paul Sabatier, 118 route de Narbonne, 31062 Toulouse cedex 9, France
[c] Laboratoire SoftMat, CNRS UMR 5623, Université de Toulouse III Paul Sabatier, 118 route de Narbonne, 31062 Toulouse cedex 9, France
[d] Université de Limoges, LABCiS UR 22722, F-87060 Limoges, France

ARTICLE INFO

Keywords:
Rhenium
Photochemistry
Nanoparticle
Cellulose nanocrystal
Singlet oxygen
Antimicrobial

ABSTRACT

Infections caused by antibiotic-resistant bacteria represent a major public health problem, and efforts continue to be made to seek new ways of addressing this issue. Photoactivatable carbon monoxide (CO)-releasing molecules (photoCORMs) could be an alternative solution to conventional antibiotics, but their mechanism of action is complex and still badly known. In the present work, a tricarbonylrhenium(I) complex (**Re-Phe(TPP)**) was developed, as well as a more hydrophobic analogue substituted by an adamantyl moiety (**Re-Ada(TPP)**). When irradiated in the near UV, these molecules generate rapidly one molecule of CO, as well as small amounts of singlet oxygen ($^1O_2$). Their decarbonylated photoproducts **D-Re-Phe(TPP)** and **D-Re-Ada(TPP)** generate only $^1O_2$, on a prolonged period of time. All these complexes were immobilized on a biocompatible cellulose nanocrystal (CNC) matrix, so that only the diffusive species (CO and $^1O_2$) may be the active ones. Finally, the bactericidal activity of all these systems was evaluated on two bacteria strains, causative of the main wound infections. No compound was active against *Pseudomonas aeruginosa*. Free **Re-Phe(TPP)** appeared to be a very good antibacterial agent in the dark against *Staphylococcus aureus*, although the same molecule adsorbed on the CNC material was ineffective, so that its activity was mainly attributed to direct biological effect. The adamantyl derivative **Re-Ada(TPP)** was more active in the presence of light than in the dark, possibly due to the contribution of CO and $^1O_2$. In contrast, the decarbonylated photoproduct **D-Re-Phe(TPP)** only showed moderate activity, suggesting that the production of $^1O_2$ is not enough to induce a significant bactericidal effect. This work allows to identify the limits of Re(I) photoCORMs and corresponding nanomaterials, which are still little used in the fight against bacteria, and it provides good indications on how to improve their design.

1. Introduction

Antibiotic-resistant bacteria have become a threat to global public health, and alternative solutions to fight them are urgently needed [1]. Carbon monoxide (CO), which is involved in multiple biological processes [2], has been identified as an inhibitor of bacteria proliferation and a potent antibacterial agent [3–5]. It could have a direct effect on the metalloproteins of the respiratory chain and on nucleic acids, as well as an indirect effect on the inflammation mechanisms that are a response to infection, thus helping the immune system to eradicate the pathogen [4]. However, since CO is a poison at high concentrations, it may be advantageous to promote its accurate delivery by using CO-releasing molecules (CORMs) [6–8]. Among the latter, photochemically-activatable CORMs (PhotoCORMs) [9–13] offer fine spatial and temporal control of the production of CO under light irradiation [7,14,15], as well as possible reporting of this activity by luminescence methods

* Corresponding author.
E-mail address: suzanne.fery-forgues@univ-tlse3.fr (S. Fery-Forgues).

https://doi.org/10.1016/j.jphotochem.2024.115600
Received 29 January 2024; Received in revised form 5 March 2024; Accepted 17 March 2024
Available online 19 March 2024

[11,16–18]. To date, the vast majority of CORMs and photoCORMs have been metal carbonyl complexes, although they exhibit complicated reactivity in biological medium [19]. unlike the totally organic compounds that have been developed recently [17,18,20]. Most of these molecules show anticancer, anti-inflammatory and cytoprotective activity [6,7,8,13,14,15,16,21,22]. Regarding antibacterial applications, CORMs have proven for a long time to be much more efficient bactericides than CO gas alone [23–25]. Multiple biological targets seem to be involved [25–35], especially in the bacterial cell envelope [31,21]. For metallic CORMs, the enhancement of the CO effect by concomitant generation of reactive oxygen species (ROS) has been proposed [36–39]. CORMs are also able to boost the effects of existing antibiotics [40–43]. For all these reasons, CORMs have raised high hopes as novel antimicrobial agents in the post-antibiotic era [14,15,21,23,24,37]. Comparatively, photoCORMs have been relatively little used for antimicrobial applications [21,34,36,37,44]. A pentacarbonyltungsten complex has shown its activity against *S. aureus* [45]. Various manganese(I) complexes have proven to be active against ESKAPE bacteria and bacterial biofilms [46], and against *E. coli* [44,47], including multi-drug-resistant forms of those bacteria [41]. As regards rhenium(I) complexes, remarkable exceptions are the bisquinoline derivatives of Frei *et al.*, which, in addition to kill *S. aureus,* display light-induced antibiotic activity against drug-resistant *E. coli* strains with minimum inhibitory concentration (MIC) values as low as 5.8 μM (4 μg.mL^{-1}) [48]. However, this small number of examples explains that the specific mode of action of photoCORMs has hardly been studied.

To the best of our knowledge, there are very few examples where CORMs and photoCORMs have been integrated to a material for antibacterial chemotherapy [49,50]. The aim is to enhance the payload of these water-insoluble molecules and trap the potentially toxic metal fragments. For instance, one Ru(II)-based CORM has been covalently associated to an organic polymer, leading to a longer action and better antimicrobial activity towards *P. aeruginosa* biofilms than the isolated molecules [51]. Besides, an electrospun nonwoven incorporating a photoresponsive Mn(I) complex has been shown to eliminate biofilms of drug-resistant *S. aureus* associated to skin wound infections [52].

Over the past few years, our team has developed a prototype of photoCORM based on a tricarbonylrhenium(I) complex that incorporates a 3-(2-pyridyl)-1,2,4-triazole ligand (called pyta ligand) with appended phenylbenzoxazole group [53]. The photodecarbonylation reaction is particularly efficient, but the tedious synthesis and purification of this compound is not adapted to a large scale production. Meanwhile, the preparation of photostable complexes that incorporate a chloride ancillary ligand and a phenyl-pyta ligand devoid of benzoxazole has been optimized. This simplified framework offers new possibility of substitution while the main physicochemical properties are maintained [54].

The aim of the present work was to develop new photoCORMs, to clarify their mechanism of action, and to estimate the value of a nanomaterial based on these compounds. In a first step, new complexes were synthesized. Based on our previous results [54], the simplified phenyl-pyta structure was retained for its excellent chelating and optical properties. Like for our photoCORM prototype [53], and according to an effective design [9,10,11,22], a triphenylphosphine (TPP) ligand, which competes with the CO ligand *trans* to it for the Re electrons and weakens the Re-C bond, was introduced to enhance the photochemical reactivity.

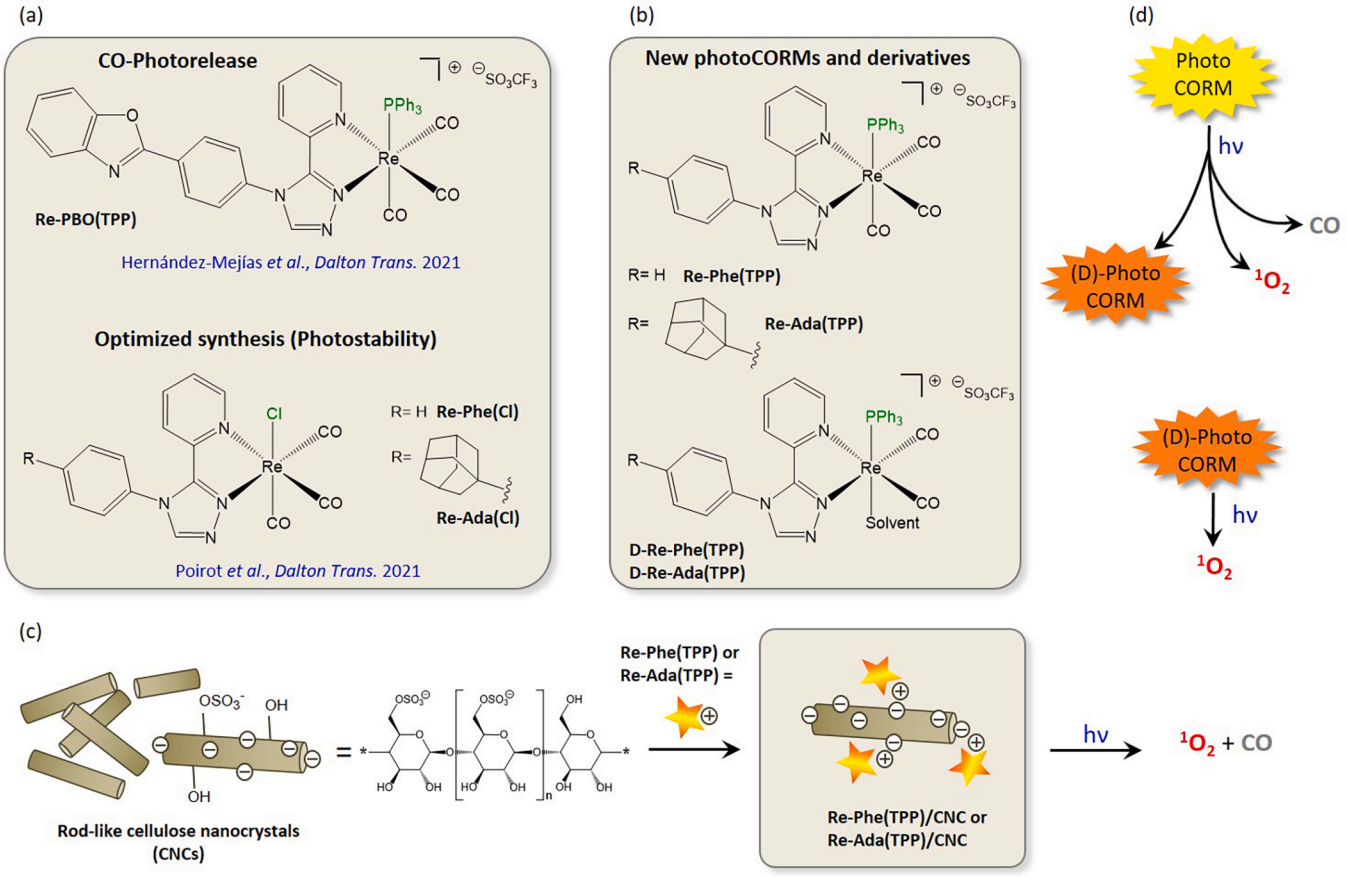

Fig. 1. A) Chemical structure of photoCORM **Re-PBO(TPP)** (top) and photochemically-stable synthetic precursors (**Re-Phe(Cl)** and **Re-Ada(Cl)**, bottom) studied in previous works (refs. [53] and [54]); b) new photoCORMs (**Re-Phe(TPP)** and **Re-Ada(TPP)**, top) and their decarbonylated photoproducts (**D-Re-Phe(TPP)** and **D-Re-Ada(TPP)**, bottom) prepared in the present work; c) Cellulose nanocrystals and preparation of the **Re-Phe(TPP)/CNC** and **Re-Ada(TPP)/CNC** hybrids by electrostatic interaction; d) Free chemical species present in the medium, including those expected from photoreaction.

Complex **Re-Phe(TPP)** (Fig. 1) bears a simple phenyl ring on the pyta moiety. In its analogue **Re-Ada(TPP)**, the phenyl ring was substituted in the *para* position by a bulky adamantyl moiety, used to increase lipophilicity and for its value in drug design [55,56]. Both molecules are positively charged and expected to generate CO upon irradiation. For the sake of comparison, the decarbonylated photoproducts **D-Re-Phe (TPP)** and **D-Re-Ada(TPP)** that can no longer produce CO were also considered. Additionally, all complexes could generate ROS, and in particular singlet oxygen ($^1O_2$). In fact, rhenium is a heavy metal that strongly enhances intersystem crossing, so that the lowest excited triplet state is easily populated and can be involved in energy transfer with dissolved dioxygen.

In a second step, the photoCORMs were immobilized on a solid support, so as to see the effect of diffusing species alone and to test the value of the resulting material. To do so, cellulose nanocrystals (CNCs) were selected. These biocompatible rod-shaped nanoparticles come from the crystalline regions of natural cellulose after hydrolysis by sulfuric acid [57–59] (Fig. 1a). Their surface brings a lot of negative charges (OSO_3^-), so that they can bind to a variety of positively-charged molecules through electrostatic interactions. CNC-based antibacterial materials have recently attracted increasing attention because of potential applications in the fields of wound dressing, drug delivery systems, food packaging, ultrafiltration, adsorbents, and textile coatings [60,61]. It has even been reported that CNCs alone show antibacterial activity due to their physical action on bacterial membranes [62]. However, to the best of our knowledge, there are no examples of association of photoCORMs with CNCs. In the present case, stable hybrids **Re-Phe(TPP)/CNC** and **Re-Ada(TPP)/CNC** were obtained and characterized.

Finally, the photochemical properties of the free complexes and nanomaterials in aqueous medium were evaluated. The antibacterial activity was measured against two bacteria strains responsible of the most dangerous infections, and an interesting effect was observed for one of them. The comparison of these various systems is an original approach that allows clarifying the mechanisms involved in the bactericidal action of photoCORMs. It gives an idea of what can be expected from photoCORM materials in this field and how they could be optimized.

2. Experimental section

2.1. Synthesis of the complexes

All purchased chemicals were of the highest purity commercially available and used without further purification. Analytical grade solvents were used as received. Experiments were carried out under a nitrogen atmosphere. Reactions were monitored by TLC on silica gel Alugram® Xtra SIL G/UV_{254}. Column chromatography was performed on Machery-Nagel silica gel or neutral alumina. NMR, mass and infrared spectra were obtained in the relevant 'Services communs de l'Institut de Chimie de Toulouse, Université de Toulouse III-Paul-Sabatier'. ^{1}H- and ^{13}C NMR spectra were recorded on a Bruker Avance 300 MHz spectrometer. Attributions of the signals were made using 2D NMR data (COSY, HSQC and HMBC). Signals are described as follow: s, singlet; d, doublet; t, triplet; m, multiplet. HRMS data were recorded on a Xevo G2 QTOF (Waters) instrument. Infrared spectra were obtained on a Nexus Thermonicolet apparatus with DTGS as the detector. Microanalyses were performed using a PerkinElmer 2400 Series II CHNS/O elemental analyzer.

General procedure for the preparation of complexes Re-Phe (TPP) and Re-Ada(TPP). The full synthesis scheme is given in Fig. S1 (ESI). The synthesis of complexes **Re-Phe(Cl)** and **Re-Ada(Cl)** has been previously described [54]. In a vessel placed under nitrogen atmosphere and protected from light, complex **Re-Phe(Cl)** or **Re-Ada(Cl)** (0.11 mmol) and silver triflate (67 mg, 0.26 mmol) in ethanol (25 mL) were heated at 80 °C for 5 h. After cooling at room temperature, the mixture was filtered using a PTFE Millipore (0.2 μm) filter. Then, triphenylphosphine (277 mg, 1.06 mmol, 10 eq.) was added to the filtrate, and the solution was heated overnight at 80 °C. After cooling at room temperature, the solution was filtered. The filtrate was dried by solvent evaporation under reduced pressure and purified by chromatography on alumina using CH_2Cl_2/MeOH 98:2 v/v as eluent to obtain a yellow solid after solvent evaporation under vacuum.

[Re(CO)$_3$(2-(4-phenyl-*4H*-1,2,4-triazol-3-yl)pyridine)(PPh$_3$)]$^+$(CF$_3$SO$_3$)$^-$ (Re-Phe(TPP)) (86 mg, Yield = 83 %). ^{1}H NMR (300 MHz, $CDCl_3$) δ (ppm): 8.64 (dd, J = 5.5, 1.5 Hz, 1H, H_1); 8.42 (s, 1H, H_7); 8.04 (td, J = 7.9, 1.8 Hz, 1H, H_3); 7.74–7.64 (m, 4H, $H_{9,10}$); 7.53 (ddd, J = 7.7, 5.5, 1.3 Hz, 1H, H_2); 7.48–7.32 (m, 10*H*, $H_{11,14,15}$); 7.23–7.13 (m, 6H, H_{13}); 6.93 (d, J = 8.0 Hz, 1H, H_4). ^{13}C NMR (75 MHz, $CDCl_3$) δ(ppm): 194.7 (d, J = 7.3 Hz, (CO)); 193.0 (d, J = 8.4 Hz, (CO)); 185.2 (d, J = 61.3 Hz, (CO)); 154.5 (C_1); 154.0 (C_6); 147.5 (C_7); 143.4 (C_5); 141.1 (C_3); 133.1 (d, J = 10.8 Hz, (C_{13})); 132.5 (C_{10}); 131.4 (C_9); 131.2 (d, J = 2.3 Hz, (C_{15})); 130.8 (C_8); 129.2 (C_2); 129.1 (d, J = 10.4 Hz, (C_{14})); 128.5 (d, J = 46.1 Hz, (C_{12})); 126.2 (C_{11}); 124.2 (C_4). ^{31}P NMR (121 MHz, $CDCl_3$) δ (ppm): 16.84. HRMS-ESI$^-$: *m/z* 148.9519 ([M]$^-$ calcd for CF_3O_3S, 148.9520); HRMS-ESI$^+$: *m/z* 753.1194 ([M]$^+$ calcd for $C_{34}H_{25}N_4O_3P^{185}Re$, found: 753.1187). IR ($CH_3CN$): $\nu_{(CO)}$ = 2042, 1955, 1929 cm^{-1}. Anal. calcd (%) for $C_{35}H_{25}N_4O_6F_3P^{185}ReS$: C 45.94, H 2.59, N 5.83; found: C 46.51, H 2.79, N 6.20.

[Re(CO)$_3$(2-(4-(4-((3r,5r,7r)-adamantan-1-yl)phenyl)-4*H*-1,2,4-triazol-3-yl)pyridine)(PPh$_3$)]$^+$(CF$_3$SO$_3$)$^-$ (Re-Ada(TPP)) (94 mg, Yield = 86 %). ^{1}H NMR (300 MHz, $CDCl_3$): δ (ppm): 8.65 (d_{app}, J = 5.4 Hz, 1H, H_1); 8.34 (s, 1H, H_7); 8.10 (t_{app}, J = 8.0 Hz, 1H, H_3); 7.65–7.58, (m, 3H, $H_{2,10}$); 7.48–7.33 (m, 11*H*, $H_{9,14,15}$); 7.17 (m, 6H, H_{13}); 6.95 (d, 1H, J = 8.1 Hz, H_4); 2.21 (m, 3H, CH_{ada}); 2.04 (m, 6H, $CH_{2\ ada}$); 1.86 (m, 6H, $CH_{2\ ada}$). ^{13}C NMR (75 MHz, $CDCl_3$): δ (ppm): 194.7 (d, J = 5.6 Hz, (CO)); 192.0 (d, J = 8.0 Hz, (CO)); 185.3 (d, J = 60.4 Hz, (CO)); 154.0 (C_6); 154.6 (C_1); 147.6 (C_7); 143.4 (C_5); 129.5 (C_2); 133.1 (d, J = 10.7 Hz, (C_{13})), 131.2 (d, J = 2.4 Hz, (C_{15})); 141.3 (C_3); 129.1 (d, J = 10.0 Hz, (C_{14})); 128.6 (d, J = 45.8 Hz, (C_{12})); 128.0 (C_8); 127.9 (C_{10}); 125.6 (C_9); 156.3 (C_{11}); 124.1 (C_4); 42.8 ($CH_{2\ ada}$); 36.8 (C_{ada}); 36.5 ($CH_{2\ ada}$); 28.7 (CH_{ada}). ^{31}P NMR (121 MHz, $CDCl_3$) δ (ppm): 16.85. HRMS-ESI$^-$: *m/z* 148.9519 ([M]$^-$ calcd for CF_3O_3S, 148.9520); HRMS-ESI$^+$: *m/z* 889.2317 ([M]$^+$ calcd for $C_{44}H_{39}N_4O_3P^{185}Re$: found: 889.2311). IR (ATR): $\nu_{(CO)}$ = 2035, 1946, 1907 cm^{-1}. Anal. calcd (%) for $C_{42}H_{39}N_4O_6F_3P^{185}ReS$: C 52.07, H 3.79, N 5.40; found: C 52.10, H 3.81, N 5.20.

2.2. Crystallography

Crystallographic data (Table 1) were collected at low temperature (193 K) on a Bruker APEX II Quazar diffractometer equipped with a 30 W air-cooled microfocus source for **Re-Ada(TPP)**, and on a Bruker D8 VENTURE diffractometer equipped with a PHOTON III detector for **Re-Phe(TPP)**, using MoK_α radiation (wavelength = 0.71073 Å). Phi and Omega scans were performed for data collection. Space group was determined on the basis of systematic absences and intensity statistics. An empirical absorption correction was employed [63]. The structures were solved using an intrinsic phasing method (ShelXT) [64]. All non-hydrogen atoms were refined anisotropically using the least-square method on F^2 [65]. Hydrogen atoms were refined isotropically at calculated positions using a riding model. Supplementary crystallographic data can be obtained free of charge from The Cambridge Crystallographic Data Centre via https://www.ccdc.cam.ac.uk/structures.

2.3. Computational details

The ORCA software was employed for all calculations (the geometry optimization, the ground-state and excited-state electronic structures, and optical spectra) with the aid of the Gabedit visualization program [66]. Density functional theory (DFT) and time-dependent DFT (TD-DFT) calculations were performed with the PBE0 functional [67]. The ground state (S_0) and the lowest excited triplet state (T_1) geometries of

Table 1
Selected crystallographic data of complexes **Re-Phe(TPP)** and **Re-Ada(TPP)**.

	Re-Phe(TPP)	Re-Ada(TPP)
Empirical formula	$C_{34}H_{25}N_4O_3PRe$, CF_3O_3S	$C_{44}H_{39}N_4O_3PRe$, CF_3O_3S
Formula weight	903.83	1038.04
Crystal system	Orthorhombic	Orthorhombic
Space group	$Pna2_1$	Pbca
Unit cell dimensions:		
a (Å)	25.935(2)	15.079(4)
b (Å)	8.8698(6)	19.276(4)
c (Å)	14.8941(12)	28.520(7)
α (°)	90	90
β (°)	90	90
γ (°)	90	90
Volume ($Å^3$)	3426.2(4)	8290(3)
Z	4	8
Density (calculated) (Mg/m^3)	1.752	1.663
Crystal size (mm^3)	0.280 × 0.200 × 0.180	0.100 × 0.080 × 0.060
Reflections collected	133492	284588
Independent reflections	14759 [R(int) = 0.0467]	14373 [R(int) = 0.1196]
Restraints/parameters	1/460	0/550
Final R1 index I > 2σ(I)	0.0167	0.0382
wR2 (all data)	0.0393	0.0921
Largest diff. peak and hole (e $Å^{-3}$)	0.899 and −0.873	1.278 and −1.190
CCDC	2298669	2298670

compounds were fully optimized with the DFT method using the Perdew-Burke-Ernzerhof PBE0 functional without symmetry constraints [68]. In all calculations, the "double-ζ" quality basis set LANL2DZ with Hay and Wadt's relative effective core potential ECP (outer-core [($5s^2 5p^6$)] electrons and the ($5d^6$) valence electrons) [69,70] was employed for the Re^+ cation. The solvent effect was simulated using the Conductor-like Polarizable Continuum Model (CPCM) [71,72]. The vibrational frequency calculations were performed using the optimized structural parameters of compounds, to confirm that each optimized structure represents a local minimum on the potential energy surface. On the basis of the optimized ground state geometry, the absorption properties were calculated by the TD-DFT method at the PBE0/LANL2DZ level. The emission has been calculated by DFT considering the difference of energy between the optimized excited triplet state and the singlet state at the same geometry. Orbital compositions have been calculated using Multifwn software [73] with the orbital composition analysis (Mulliken partition) function [74].

2.4. Spectroscopy

When not specified, spectroscopic measurements in solutions were performed at 20 °C on undegassed solutions using temperature-controlled cells of 1 cm optical pathway. UV–visible absorption spectra and steady-state emission spectra were measured with a Xenius SAFAS spectrofluorometer. All emission spectra were corrected. The emission quantum yields (Φ) were determined using the classical formula:

$$\Phi_x = (A_s \times I_x \times n_x^2 \times \Phi_s)/(A_x \times I_s \times n_s^2) \quad (1)$$

where *A* is the absorbance at the excitation wavelength, *I* the integrated emission intensity and *n* the refractive index. Subscripts *s* and *x* refer to the standard and to the sample of unknown quantum yield, respectively. Coumarin 153 ($\Phi_s = 0.53$) in ethanol was used as the standard [75]. The absorbance of the solutions was equal or below 0.06 at the excitation wavelength. The error on the absorptivity and quantum yield values is estimated to be about 10 %. The solubility limits of the complexes in the water/acetonitrile 96:4 v/v mixture were determined by monitoring the variation of absorptivity *vs.* the complex concentration. Cells of 1 cm and 1 mm optical pathway were used for this work.

Emission decay curves of dilute solutions (Abs at $\lambda_{ex} < 0.1$) were recorded using the time-correlated single photon counting method (TCSPC) on a Horiba Fluorolog 3–2iHR320 spectrofluorometer equipped with a Nanoled-370 (λ_{ex} = 371 nm). Emitted photons were detected at 90° by means of a Hamamatsu R928 photomultiplier. Emission was recorded near the maximum with a bandpass of 4 nm. The instrumental response was recorded directly by measuring the scattering of the sample at 370 nm before each decay curve. All analyses were recorded using the Datastation v2.7 software from Horiba. The decay curves were analyzed with reconvolution and global non-linear least-squares minimization method using the DAS6 v6.8 software, also from Horiba.

The photophysical radiative (k_r) and non-radiative (k_{nr}) rate constants were calculated as: $k_r = \Phi/<\tau>$ and $k_{nr} = (1\text{-}\Phi)/<\tau>$, with Φ the emission quantum yield and $<\tau>$ the average lifetime.

2.5. Preparation and characterization of the nanomaterials

Synthesis of cellulose nanocrystals (CNCs). Cellulose nanocrystals (CNCs) were obtained according to the method developed by Ndong Ntoutoume *et al.* [76]. Hydrophilic cotton (5 g) and 125 mL of 64 % sulfuric acid were heated to 50 °C for 1 h30. The reaction was stopped with 625 mL of ultrapure water and cooled to room temperature. The crude product was centrifuged (4,000 rpm, 15 min, 3 times) to eliminate the limpid supernatant. The pellet was redispersed in deionized water until obtention of a slightly bluish and troubled supernatant. This supernatant was sonicated for 5 min, filtered and dialyzed (6–8 kDa) for 4 days by changing ultrapure water 3 times a day to obtain a stable colloidal suspension of CNCs (0.4 L, 4.4 $mg.mL^{-1}$, yield = 35 %). FTIR (KBr): $\nu_{(OH)} = 3338\ cm^{-1}$, $\nu_{(CH)} = 2900\ cm^{-1}$, $\nu_{(OH)} = 1642\ cm^{-1}$, $\nu_{(SO_3H)} = 1279\ cm^{-1}$, $\nu_{(C\text{-}O\text{-}C)} = 1162\ cm^{-1}$, $\nu_{(SO_3H)} = 816\ cm^{-1}$.

Preparation of PhotoCORM/CNC hybrids. Small volumes of a concentrated solution (2×10^{-3} M) of complexes **Re-Phe(TPP)** and **Re-Ada(TPP)** were poured into aqueous suspensions of CNCs (2.1 mg/mL, except if indicated differently in the text) under magnetic stirring. The proportion of acetonitrile in water was 4 %. The mixtures were left to stir in the dark at room temperature for 1 h, then overnight without stirring. They were sonicated 5 min before spectroscopic measurement.

Dynamic light scattering (DLS). Average hydrodynamic diameters and polydispersity indices were measured by dynamic light scattering (DLS) with a Malvern Zetasizer Nano-ZS. Zeta-potential data were measured with the same apparatus by using the electrophoretic light scattering method (150 V). Measurements were made on the pellet collected after centrifugation of the samples and dispersed again in water, to limit contamination by unbound complexes. Each sample was

analyzed in triplicate at 20 °C in a temperature-controlled cell. Pure water was used as reference.

Transmission electron microscopy. TEM was performed on a JEOL JEM-1011 electron microscope operating at 100 kV and equipped with a wide-angle Megaview III camera. An aqueous suspension of **Re-Ada (TPP)/CNC** hybrid was vortexed and sonicated for 2 min, then a drop was deposited on a carbon-coated grid. The excess liquid was drained off and the sample was dried under vacuum (10^{-4} mbar) at room temperature. No contrast agent was added.

Determination of the maximum adsorption capacity (MAC) by absorption spectroscopy. Samples containing 7.28×10^{-5} M (65.75 mg/L) and 1.02×10^{-4} M (106.35 mg/L) of **Re-Phe(TPP)** or **Re-Ada (TPP)**, respectively, and variable amounts of CNCs ranging from 0 to 1 mg/mL were prepared in water/acetonitrile 96:4 v/v as described above. The samples were centrifuged for 15 min at 10,000 rpm, and the absorbance of the supernatant was measured at 340 nm. Beer-Lamber's law allowed the corresponding photoCORM concentration to be obtained. The photoCORM concentration in the supernatant corresponds to the value [C_0 - C_{ads}], where C_0 is the initial concentration and C_{ads} the concentration of adsorbed complex. This value was then plotted as a function of [CNC]. The maximum adsorption capacity was given by the C_{ads} value at the point where the slope reaches a plateau.

Complex release from photoCORM/CNC hybrids

Method 1. A dialysis tube from a Pur-A-Lyzer™ Maxi 3500 kit purchased from Sigma Aldrich was loaded with 3 mL PhotoCORM/CNC hybrid suspension containing 2.0 mg/mL CNCs and 1.2×10^{-4} M **Re-Phe (TPP)** or 8.3×10^{-5} M **Re-Ada(TPP)**, and then it was placed into a tank containing 200 mL of ultra-pure water. The absorbance of the content of the dialysis cell was monitored over time. Alternatively, the emission of the dialysis solution was measured by luminescence spectroscopy over 24 h, and the amount of released complex was determined using a calibration curve.

Method 2 [76]. A volume (2 mL) of chloroform was topped with 1 mL of photoCORM/CNC hybrid suspension containing 2 mg/mL CNCs and 1.84×10^{-4} M **Re-Phe(TPP)** or 6.93×10^{-5} M **Re-Ada(TPP)** into a quartz cell, so that the beam from the spectrometer passes only through the organic phase. The system was left to stand without stirring. The diffusion of complex from the aqueous phase to the organic phase was monitored every hour for 24 h, by measuring the absorbance of the organic phase.

2.6. Photochemistry

Irradiations were conducted at 20 °C on magnetically-stirred undegassed solutions placed in 1 cm × 1 cm quartz fluorescence cells, using a Rayonet reactor fitted with 350 nm UV lamps. The CO-photorelease was monitored by UV–vis spectroscopy. The quantum yields of CO-photoproduction (Φ_{CO}) were determined using the equations:

$$A_0 = C_0 \times \varepsilon_{complex} \quad (2)$$

$$A_f = C_0 \times \varepsilon_{photoproduct} \quad (3)$$

$$A_t = (C_0 - x) \times \varepsilon_{complex} + x \times \varepsilon_{photoproduct} \quad (4)$$

$$\Phi_{CO} = N_x / N_{abs} \quad (5)$$

where A_0, A_f, A_t are respectively the absorbance values at 340 nm before, during and after irradiation; C_0 is the initial concentration in complex, $\varepsilon_{complex}$ and $\varepsilon_{photoproduct}$ are the molar extinction coefficients at 340 nm of the complex and photoproduct, x refers to the concentration of the photoproduct at time t; N_x is the number of photolyzed molecules and N_{abs} is the number of absorbed photons. The number of photons received by the samples was measured to be 3.6×10^{16} photons.s^{-1} by actinometry of ferrioxalate ions [77].

The production of singlet oxygen was quantified according to the method of Kraljic and El Mohsni [78]. By reacting with the singlet oxygen formed, *L*-histidine (His) gives an intermediate which causes the bleaching of *N,N*-dimethyl-4-nitrosoaniline (RNO), according to the following process:

$$^1O_2 + \text{His} \longrightarrow [\text{HisO}_2] \longrightarrow \text{HisO}_2$$

$$[\text{HisO}_2] + \text{RNO} \longrightarrow \text{RNO}_{\text{bleached}} + \text{by-products}$$

The decrease of the RNO absorption band at 440 nm as a function of time allows the reaction progress to be monitored. The experiment was repeated twice for each sample. Slopes were determined from the spectra after baseline correction and ignoring the first points (<3 min) for which the RNO absorbance decrease and the photoproduct absorption increase overlap. Then, the singlet oxygen quantum yields (Φ_Δ) were calculated by using equation (6):

$$\Phi_{\Delta s} = \Phi_{\Delta ref} \times S_s / S_{ref} \times A_{ref} / A_s \quad (6)$$

where ϕ_Δ is the quantum yield, S is the slope of the absorbance variation recorded at 440 nm, and A is the absorbance at the irradiation wavelength of 350 nm for the sample (*s*) and the reference (*ref*). The reference compound was erythrosin B in H_2O ($A_{ref} = 0.0386$, $\Phi_{\Delta ref} = 0.63$), and very close results were obtained using Rose Bengal [79]. For the complexes and photoCORM materials, experiments were carried out in a water/acetonitrile (96:4 vol/vol) mixture, which was approximated to pure water for the calculations.

2.7. Bacteriological studies

Gram-positive (*S. aureus* CIP76.25) and Gram-negative (*P. aeruginosa* CIP76.110) bacterial strains were purchased from Institut Pasteur Collection (Paris, France). Bacteria were incubated for 24 h at 37 °C in liquid tryptic soy broth (TSB) (tryptone 17 g.L^{-1}, soy papain peptone 3 g.L^{-1}, dextrose 2.5 g.L^{-1}, NaCl 5 g.L^{-1}, and K_2HPO_4 2.5 g.L^{-1}) purchased from Biokar Diagnostics, under aerobic conditions. Then, the optical density of the planktonic bacterial culture was measured at 600 nm. Prior to use, an aliquot of the bacteria suspensions was dispersed in phosphate buffered saline (PBS) to obtain a final concentration of ~ 2×10^6 colony-forming units (CFU). The inoculum was then centrifuged for 3 min at 10,000 rpm, and the pellet was redispersed in PBS. The washing procedure, which allows to get rid of dead cells and residues from the TSB medium, was repeated twice.

The minimal inhibitory concentrations (MIC) were determined by using the microdilution method. All experiments were performed in triplicate (biological and experimental repeats). For free photoCORMs, an acetonitrile solution of rhenium complexes was added to PBS, and the resulting mixture was sonicated for 3 min. It contained 10 % v/v acetonitrile. PhotoCORM/CNC hybrids were prepared by bringing together a solution of photoCORM in acetonitrile (100 µL, 2×10^{-3} M) and a suspension of CNCs in water (900 µL, 2.1 g/L). The final medium contained 10 % acetonitrile v/v. After standing overnight in the dark, the suspension was centrifuged for 10 min at 10,000 rpm and the pellet was redispersed in PBS. The procedure was repeated twice before dilution in this medium. The sample was finally sonicated for 3 min before use. Aliquots (50 µL) of photoCORMs and hybrids of increasing concentrations were deposited into the wells of a 96-round-bottomed well plate (Costar Assay), and 50 µL of PBS was added. Bacteria suspensions (50 µL, 2×10^6 CFU mL^{-1}) were finally deposited in each well. The concentrations of photoCORMs, whatever free or adsorbed on the CNC surface, ranged between 125 µM and 1 µM, and the proportion of acetonitrile in PBS was lower than 10 % v/v. The plate was incubated for 1 h at 37 °C, and then irradiated for 10 min at 365 nm using a Vilber Lourmat™ UV lamp (3.38 W.m^{-2}). Straight after, 2-fold concentrated TSB (100 µL) was added in each well and the plate was incubated for 24 h at 37 °C. The opacity of the well, which reflects bacterial growth, allowed the MIC to be visually determined. Other plates, prepared under

the same conditions but without irradiation, were used as control. Supplementary controls were made with Methylene Blue dye (MB, Merck, Saint-Quentin-Fallavier, France) and Gentamicin (Merck). MB was solubilized in PBS and was incubated with bacteria at concentrations between 125 μM and 1 μM. After incubation in the dark for 1 h at 37 °C, bacteria were irradiated with white light LED at a total fluence of 25 J.cm^{-2} (Lumidox® II 96-Well LED Arrays, Analytical Sales and Service, Flanders NJ, USA). As previously, 2-fold concentrated TSB was added in each well. Gentamicin was solubilized in PBS and was incubated with bacteria at concentrations between 125 μM and 1 μM. 2-Fold concentrated TSB was added in each well and plates were incubated for 24 h at 37 °C.

To measure the minimal bactericidal concentration, serial dilutions of the content of each well were performed. Each dilution was spread on tryptic soy agar plates using an automatic plate. After incubation at 37 °C for 24 h, the plates were counted to determine the total CFU per mL (CFU.mL^{-1}). Due to the protocol employed, the lowest concentration was about 300 CFU.mL^{-1}. All negative controls (buffer alone, bacteria without added compound) in the presence or absence of illumination, were made systematically.

3. Results and discussion

3.1. Synthesis, characterization and crystal structure of complexes *Re-Phe(TPP)* and *Re-Ada(TPP)*

The complexes **Re-Phe(TPP)** and **Re-Ada(TPP)** were obtained in one step by reacting the corresponding chloride analogue [54] with silver triflate, and then with triphenylphosphine, with a good yield of 83 % and 86 %, respectively, after purification by column chromatography (Fig. S1). There were identified by ^{1}H and ^{13}C NMR (Fig. S2-S11, ESI), high resolution mass spectrometry, and their purity was checked by elemental microanalysis. The Fourier transform infrared (FTIR) spectra showed the stretching bands that are the characteristic signature of the three CO groups in a *fac*-[Re(CO)$_3$] arrangement.

Good quality single crystals were formed at the interface between pentane and a chloroform solution of complexes **Re-Phe(TPP)** and **Re-Ada(TPP)**, and the XRD analysis allowed the structures to be confirmed (Fig. 2 and Table S1). The coordination spheres of both complexes are almost similar. They exhibit a slightly-distorted octahedral geometry, in which the rhenium atom is coordinated to three carbonyl groups in a *fac* configuration, two nitrogen atoms of the pyta ligand and one phosphorous atom. A remarkable feature is that the Re-C(1) bond involving the carbonyl ligand that faces the phosphorous atom is significantly longer than the Re-C(2) and Re-C(3) bonds of the other two carbonyls (*e.g.* 1.971(2) *vs* 1.920(2) and 1.926(2) Å for **Re-Phe(TPP)**). It is also longer than its counterpart in the chloride parent complex (1.916(3) Å) [54], and this reflects its weakening due to the electronic effect of the TPP moiety. The angles of the coordination sphere are close to orthogonal and the pyta moiety is almost planar, a geometry probably favored by the steric hindrance due to the TPP moiety. Noticeably, one of the TPP phenyl rings is positioned more or less parallel to the pyta moiety. The shortest C_{phenyl}-C_{pyta} distance is 3.362(3) Å for **Re-Phe(TPP)** and 3.388(5) Å for **Re-Ada(TPP)**. Although no overlap of the aromatic rings is observed and the centroid-to-centroid distance is longer than 4 Å (Fig. S12), this interaction may contribute to the stabilization of the molecules [80–82]. The dihedral angle between the phenyl (borne by the triazole) and the triazole ring, which is a strong indicator of the molecular geometry, has a value of 74.31(8)° for **Re-Phe(TPP)** and only 59.70(13)° for **Re-Ada(TPP)**. The intermolecular arrangement is strongly structured by the TPP moieties. For instance, the TPP moiety of one **Re-Phe(TPP)** molecule is involved in short contacts with the carbonyl ligands of two neighboring molecules (Fig. S13a,c), while the **Re-Ada(TPP)** molecules form sort of antiparallel dimers stabilized by CH···C bonds between the phenyl rings of their TPP moieties (Fig. S13b, d). The crystal unit of **Re-Phe(TPP)** contains four molecules oriented in distinct directions. In the network of **Re-Ada(TPP)**, the molecules are displayed along two distinct axes. The presence of the bulky adamantyl moiety does not lead to an increased distance between the rhenium centers of neighboring molecules (8.869(1) Å for **Re-Phe(TPP)** *vs.* 8.068 (2) Å for **Re-Ada(TPP)**).

3.2. Electronic properties of complex *Re-Phe(TPP)*

A previous study on the parent chloride complexes showed that the presence of the adamantyl substituent does not influence significantly the electronic properties in solution [54]. Consequently, theoretical calculations only considered complex **Re-Phe(TPP)** in acetonitrile. They were made using the density functional theory (DFT) and time-dependent DFT (TD-DFT) methods. The results are collected in Table S2 and S3, and in Fig. S14-17). In the ground state, the geometry of the molecule is close to that determined from X-ray analysis (Fig. S14). The electron density of the four highest occupied molecular orbitals is mainly centered on the rhenium atom (Fig. S15). The contribution of the phosphine ligand is strong, especially between HOMO-6 and HOMO-2. The contribution of the carbonyl ligands is moderate, while that of the pyta moiety only becomes significant for the HOMO-1 and HOMO. Regarding the lowest unoccupied molecular orbitals, the electron distribution is concentrated on the pyta ligand for the LUMO and LUMO + 1, and then it progressively shifts to the carbonyl ligands and then to the

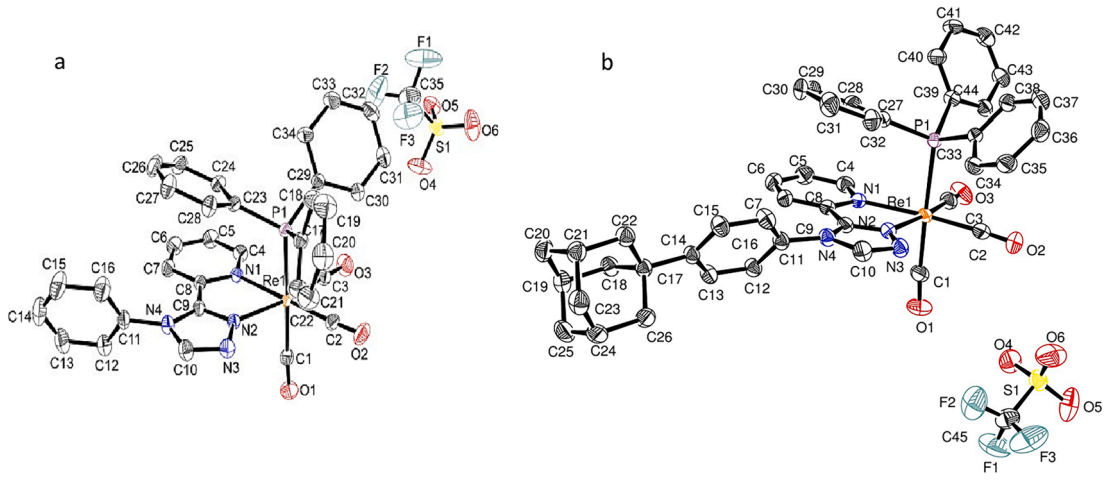

Fig. 2. Molecular view of the asymmetric unit of complexes **Re-Phe(TPP)** (a) and **Re-Ada(TPP)** (b). Displacement ellipsoids are drawn at 50% probability and hydrogen atoms are been omitted for the sake of clarity.

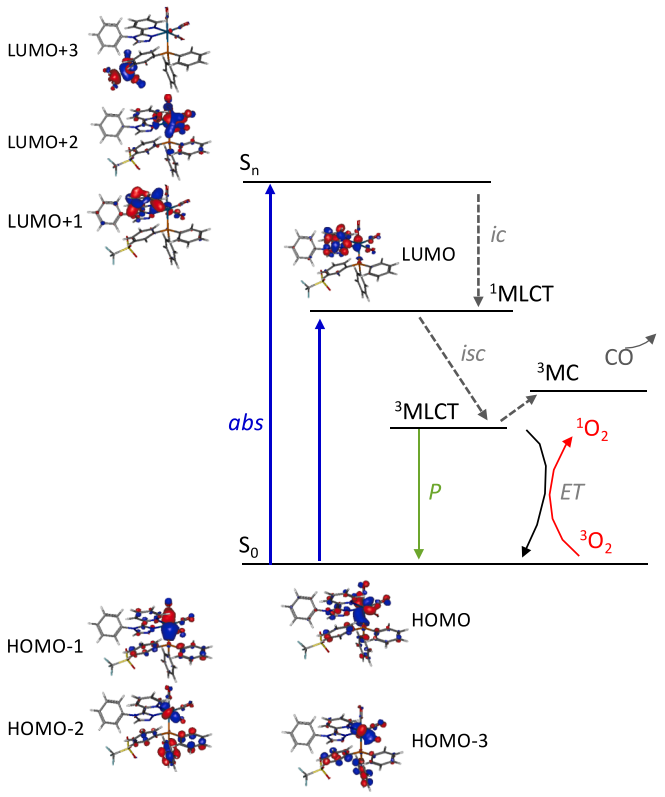

Fig. 3. Schematized energy levels, main transitions and photochemical processes of complex **Re-Phe(TPP)** in CH_3CN. Isodensity plots (isovalue = 0.03 e bohr^{-3}) of the first frontier molecular orbitals involved in some of these processes, according to TD-DFT calculations at the PBE0/LANL2DZ level of theory. *abs*: absorption, *ic*: internal conversion, *isc*: intersystem crossing, *P*: phosphorescence, *ET*: energy transfer, S: singlet, MLCT: metal-to-ligand charge transfer, MC: metal-centered.

rest of the molecule as the orbital number increases. Remarkably, the phenyl group does not participate below the LUMO + 5. This distribution is quite different from that of **Re-PBO(TPP)**, in which the electron density of the HOMO and LUMO + 1 is strong on the PBO moiety [53]. Predicted electronic transitions at low energy are mainly HOMO → LUMO and HOMO-3 → LUMO, with strong metal to ligand charge transfer (MLCT) and ligand-to-ligand charge transfer (LLCT) character. They should result in an absorption band of moderate intensity at around 350 nm (Fig. S16). The next transitions are identified as HOMO-1 → LUMO + 1 and HOMO-2 → LUMO + 1, with mixed MLCT/LLCT character. They are expected to give an intense band around 265 nm. High-energy transitions, such as HOMO-3 → LUMO + 3, with MLCT character, should be responsible for absorption below 230 nm. The main transitions and orbitals involved are given in Fig. 3.

In the lowest-energy excited triplet state, the geometry of the molecule is a little different from that of the ground state, with a reduced phenyl-pyta dihedral angle (55.8° instead of 85.6°) (Fig. S14). This is a MLCT state, in which the electron density is centered on the pyta ligand with contribution of the rhenium atom and carbonyl ligands (Fig. S17).

It should be noted that theoretical calculations were only here to better understand the absorption and emission processes. To provide a comprehensive view of the system, Fig. 3 also represents the photoproduction of singlet oxygen due to energy transfer, and the photochemical process that leads to decarbonylation. The latter process involves a metal-centered, thermally-accessible triplet state [9,10], whose energy was not calculated. This calculation requires a substantial work, and will be included in a forthcoming study, the aim of which is to compare a series of rhenium(I) photoCORMs.

3.3. Spectroscopic and CO-photoproduction properties of the complexes in solution

The complexes **Re-Phe(TPP)** and **Re-Ada(TPP)** were well soluble in acetonitrile. This hydrophilic coordinating solvent is frequently used in photochemistry and well tolerated by living cells at small concentrations. A spectroscopic and photochemical study was first conducted in this solvent, which allows to obtain precise data, directly comparable with those previously acquired for **Re-PBO(TPP)** in the same conditions. Only aerated solutions were considered. As expected, both complexes had similar spectroscopic features (Table S4). The absorption spectra (Fig. S18) showed an intense band with many shoulders below 300 nm, and a well-distinct band of moderate intensity peaking around 340 nm. For **Re-Phe(TPP)**, the experimental spectrum was in quite good agreement with the calculated spectrum (Fig. S16), and this allows in particular the low-energy band to be assigned to a transition involving the ^{1}MLCT state. When illuminated by UV light, the yellow solutions of **Re-Phe(TPP)** and **Re-Ada(TPP)** emitted green-yellow light. The emission spectra (Fig. S18) showed one only band peaking at 540 and 536 nm, respectively, in perfect agreement with the value calculated for emission arising from the lowest MLCT excited triplet state (541 nm) for **Re-Phe(TPP)**. The emission quantum yields were close to 0.04 and the lifetimes (Fig. S19) were longer than 200 ns, confirming that emission is due to phosphorescence. These spectroscopic characteristics are close to those of **Re-PBO(TPP)** (see Table S4 for a comparison).

The photochemical reactivity was investigated on **Re-Phe(TPP)**. While an acetonitrile solution of this compound kept in the dark for 15 days exhibited no change of its UV–vis absorption spectrum, irradiation

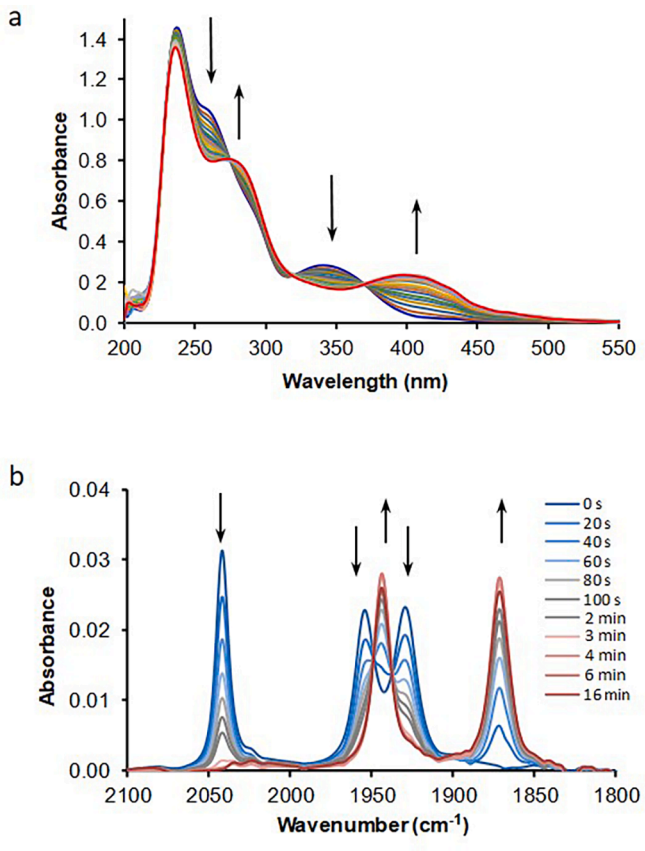

Fig. 4. a) Evolution of the UV–vis absorption spectra of **Re-Phe(TPP)** (5.6×10^{-5} M) in acetonitrile under irradiation at 350 nm. One curve every 10 s for 3 min, then one curve every min till 6 min. b) Variation of the FTIR spectra of **Re-Phe(TPP)** under irradiation at 350 nm. The arrows indicate the sense of the variation.

at 350 nm induced the fast disappearance of the bands at 260 and 340 nm, and the appearance of new bands around 280 and 400 nm. These variations indicate a major change in the coordination sphere. The formation of clear isosbestic points suggests the consumption of the starting complex and the formation of one photoproduct (Fig. 4a). After 4 min, the absorption spectra superimpose, indicating the end of this photoreaction. The kinetics was studied by monitoring the absorbance decrease at 340 nm. The reaction follows a first order kinetics with a rate constant of $k = 0.0125\ s^{-1}$. This value is useful to compare the photoreactivity of compounds used under the same experimental conditions. The photoreaction quantum yield, which allows a comparison with literature data, was measured to be 0.06. The photoreaction can also be monitored by the disappearance of the emission band at 540 nm and the appearance of a very weak band in the red at 680 nm ($\Phi_P \sim 8 \times 10^{-3}$) (Fig. S20). The photoproduct was characterized by high-resolution mass spectrometry (HRMS-ESI$^+$), which indicates the presence of a main compound corresponding to the formula $C_{35}H_{28}N_5O_2PRe$ (experimental: $m/z = 768.1544$, calculated for $[M]^+$: $m/z = 768.1538$ with ^{187}Re), *i.e.* to a complex where a carbonyl ligand has been replaced by an acetonitrile molecule (Fig. S21). Monitoring the photoreaction by infrared spectroscopy showed a strong variation of the signals corresponding to the carbonyl groups (Fig. 4b). The three bands at 2045, 1955 and 1930 cm^{-1} disappeared and were replaced by two bands at 1950 and 1870 cm^{-1}. The photochemical reaction is indeed a very efficient monodecarbonylation that can be written as:

$$[Re(CO)_3(L1)(PPh_3)]^+ \ (CF_3SO_3)^- \xrightarrow[CH_3CN]{h\nu} [Re(CO)_2(CH_3CN)(L1)(PPh_3)]^+ \ (CF_3SO_3)^- + CO$$

where L1 is the phenyl-pyta ligand. The decarbonylated complex can be abbreviated as **D-Re-Phe(TPP)** with acetonitrile as one of the ligands (Fig. 1). According to the literature [9,10] and to the DFT calculation performed in our previous work [53], its most stable form should be the one with the solvent molecule replacing the CO ligand in the *trans* position with respect to the TPP moiety. The photochemical behavior of **Re-Phe(TPP)** is therefore strongly reminiscent of that previously reported for **Re-PBO(TPP)**, except that the reaction is about twice slower in the present case (Table S4). However, it remains very effective and fully justifies the choice of the simplified compound **Re-Phe(TPP)**.

In a second step, the complexes were studied in aerated aqueous medium. To do so, they were first dissolved in acetonitrile, and small volumes of this concentrated solution were injected into water. The solubility limits in the resulting water/acetonitrile 96:4 v/v mixture were found to be about 1.0×10^{-4} M and 2.5×10^{-5} M for **Re-Phe(TPP)** and **Re-Ada(TPP)**, respectively (Fig. S22). It was checked that the UV–vis absorption spectrum of complex **Re-Phe(TPP)** was unchanged in the dark for at least 15 days, showing the good chemical stability of the compound in the presence of water. The spectroscopic properties in the water/acetonitrile 96:4 v/v mixture (Table 2) were quite close to those previously recorded in acetonitrile. Interestingly, phosphorescence was not extinguished in the aqueous mixture. On the contrary, the quantum yields were 1.5 times higher than in acetonitrile and the lifetimes (Fig. S23 and S24) were multiplied by 2.5. Knowing that dioxygen is the main phosphorescence quencher in solution, this result can be partly explained by the lesser amount of this gas dissolved in air-equilibrated water (generally considered to be around 8 mg/L) than in acetonitrile (2.42 mM, that is 38.7 mg/L [83]).

Upon irradiation, the complexes dissolved in the water/acetonitrile 96:4 v/v mixture behaved qualitatively as in acetonitrile. The intensity of the ^{1}MLCT band of the UV–vis absorption spectrum decreased abruptly while a new band appeared at around 400 nm. The high-energy band also exhibited an intensity decrease while a shoulder appeared at around 280 nm. Quasi-isosbestic points testified the formation of one main photoproduct. After less than 2 min irradiation, no more variations of the UV–vis absorption spectrum were noticed (the spectrum of **Re-Phe(TPP)** is given in Fig. S25a). The photoreaction was thus even faster than in acetonitrile. The resulting solution had lost its green phosphorescence and emitted very weakly in the red under the UV lamp (Fig. S25b). This caused the disappearance of the emission band at 542 nm and the appearance of a weak band in the red ($\lambda_{max} = 696$ nm, $\Phi_P \sim 2 \times 10^{-3}$) (Fig. S25c,d). Surprisingly, the high-resolution mass spectrum of the photolyzed solution indicated the disappearance of the starting compounds and the presence of a photoproduct identical to that obtained in pure acetonitrile, *i.e.* a tricarbonylrhenium(I) complex where one carbonyl ligand (most likely that in *trans* of the phosphine) has been replaced by a CH_3CN molecule (Fig. S26). This result was unexpected because the capacity of coordination of water with transition metals is generally higher than that of acetonitrile [84]. A preferential solvation of the complexes by acetonitrile could be an explanation.

Table 3
Physical characteristics of plain CNCs and photoCORM/CNC hybrids. Maximum adsorption capacity (MAC), hydrodynamic diameter (D_h), polydispersity index (PDI), zeta potential (ζ). Hybrid composition: **Re-Phe(TPP)** (8.0×10^{-5} M) or **Re-Ada(TPP)** (6.7×10^{-5} M), and CNCs (1.9 mg/mL).

Compound	MAC (mg/g)	D_h (nm)	PDI	ζ (mV)
CNCs	—	127 ± 1	0.169 ± 0.002	−24.3 ± 0.3
Re-Phe(TPP)/CNC	180	155 ± 3	0.177 ± 0.004	−19.1 ± 0.1
Re-Ada(TPP)/CNC	868	560 ± 51	0.378 ± 0.056	−18.2 ± 0.4

Table 2
Spectroscopic and photochemical data of the two photoCORMs and corresponding hybrids in water/acetonitrile 96:4 v/v. Maximum wavelength of absorption (λ_{abs}) and molar extinction coefficient (ε), *sh* = shoulder. Maximum emission wavelength (λ_P), phosphorescence quantum yield (Φ_P), emission lifetime (τ) with relative amplitude, average lifetime ($<\tau>$) and chi square (χ^2) values; Complex concentrations for emission: ~1.8×10^{-5} M, $\lambda_{ex} = 370$ nm. Photophysical radiative (k_r) and non-radiative (k_{nr}) rate constants. Photodecarbonylation rate constant (k_{CO}), photodecarbonylation quantum yield (Φ_{CO}). Quantum yield of singlet oxygen production of the corresponding decarbonylated compound (Φ_Δ). For hybrids: [CNC] = 1.0–2.0 mg/mL, [PhotoCORM] = 1.6×10^{-5} – 4.9×10^{-5} M. *nd*: not determined.

Compound	λ_{abs} (nm)	ε ($M^{-1}cm^{-1}$)	λ_P (nm)	Φ_P	τ (ns)	$<\tau>$ (ns)	χ^2	k_r	k_{nr}	k_{CO} (s^{-1})	Φ_{CO}	Φ_Δ
Re-Phe(TPP)	236 260*sh* 342	23,700 15,300 4100	542	0.061	591	591	1.13	1.03×10^5	1.59×10^6	7×10^{-3}	0.060	0.063
Re-Ada(TPP)	234 260*sh* 340	23,400 13,800 3800	536	0.060	583	583	1.29	1.03×10^5	1.61×10^6	8×10^{-3}	0.059	0.048
Re-Phe(TPP)/CNC	240 338	26,000 5300	526	0.042	606 (93.2 %) 53 (4.9 %) 0.93 (1.87 %)	567	1.39	7.41×10^4	1.69×10^6	5×10^{-3}	*nd*	0.040
Re-Ada(TPP)/CNC	236 338	27,000 5900	528	0.052	826 (83.9 %) 108 (11.4 %) 0.54 (4.67 %)	705	1.28	7.35×10^4	1.34×10^6	3×10^{-3}	*nd*	0.041

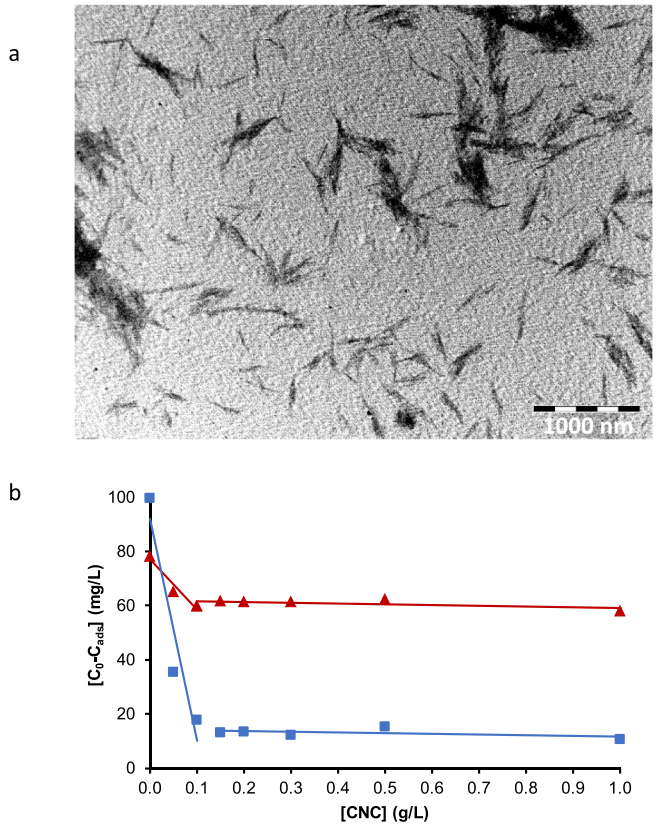

Fig. 5. A) TEM image of the **Re-Ada(TPP)** hybrid. b) Determination of the maximal adsorption capacity of CNCs for complexes **Re-Phe(TPP)** (7.3×10^{-5} M) (red triangles) and **Re-Ada(TPP)** (1.0×10^{-4} M) (blue squares). (For interpretation of the references to colour in this figure legend, the reader is referred to the web version of this article.)

3.4. Preparation and characterization of the photoCORM/CNC hybrids

To prepare the hybrids, the acetonitrile solutions of the complexes were poured into aqueous CNC suspensions under magnetic stirring, while fixing at 4 % the proportion of acetonitrile in water. The samples were left to stabilize one night before use. The hybrids were first characterized by dynamic light scattering (DLS). The hydrodynamic diameter was slightly larger for the **Re-Phe(TPP)/CNC** hybrid than for native CNCs (155 ± 3 nm *vs* 127 ± 1 nm). A significantly higher value (560 ± 51 nm) was found for the **Re-Ada(TPP)/CNC** hybrid, possibly due to some agglomeration of the nanoparticles, as suggested by the high polydispersity index. In both cases, the zeta potentials of the hybrids were found to be slightly less negative than for native CNCs (Table 3). These variations are in line with the binding of the positively-charged complex molecules at the surface of CNCs. Weaker interactions like hydrogen bonding, possibly involving the OH groups of cellulose, can also take place. The interaction did not change significantly the morphology of the CNCs, which appeared as rod-like particles under the transmission electron microscope (Fig. 5a).

From a spectroscopic point of view, CNC suspensions are opalescent and generate strong scattering (Fig. S27). As far as can be estimated despite the difficulty of the measurement, the interaction of the complexes with CNCs only led to small changes in the position of the spectra with respect to aqueous solutions, but it induced an absorbance increase particularly noticeable when **Re-Ada(TPP)** was used above the solubility limit, suggesting that CNCs improve the dispersion of the photoCORM molecules (Table 2). The emission maxima were shifted to short wavelengths (Fig. S28). Meanwhile, the emission quantum yields were slightly reduced with respect to aqueous solutions while the lifetimes were longer, mainly resulting in the reduction of the radiative constants. Possibly, the geometry of the complexes varies upon adsorption on the CNC surface, making emission slightly less efficient.

The variation of absorbance at 340 nm was monitored as a function of CNC concentration to determine the maximal adsorption capacity (MAC) of CNCs, which was found to be 172 mg/g for **Re-Phe(TPP)**, and as high as 868 mg/g for **Re-Ada(TPP)** (Fig. 5 and S29). Titration by fluorescence spectroscopy, which is more delicate to implement, was performed for **Re-Phe(TPP)**, and led to a slightly lower value (110 mg/g) than that determined by absorption spectroscopy (Fig. S28). These relatively high MAC values can be partly explained by the high molecular weight of rhenium complexes, adsorbed on a light matrix. However, it is noteworthy that the presence of the adamantyl moiety significantly increases the affinity of the complexes for CNCs.

Since sufficient time was observed between the preparation of hybrids and their use, the spectroscopic properties of the suspensions changed little over time, suggesting a good stability in water as long as the concentration conditions are maintained. However, upon dilution, a proportion of the complexes could be released in the medium. This phenomenon was studied by using two distinct methods. First, dialysis was performed by putting 3 mL PhotoCORM/CNC hybrid suspension into a dialysis cell, placed into a tank containing 200 mL of water. The progressive absorbance decrease of the cell content showed that 85 % of adsorbed **Re-Phe(TPP)** has migrated into the aqueous phase after 8 h. In contrast, 28 % of **Re-Ada(TPP)** passed into the water after one hour, and then the system seemed to be stable (Fig. S30). Detection by fluorescence spectroscopy of the dialysis solution confirmed that more than 73 % of **Re-Phe(TPP)** was released from the hybrids into the aqueous medium after 8 h, and indicated that the whole complex was released after 24 h (Fig. S31). The second method measures the desorption of complexes and their solubilization into an organic phase by UV–vis absorption titration (Fig. S32). It is assumed that it better models what happens in the presence of a lipid membrane [76]. In this case, 31 % of **Re-Phe(TPP)** and 27 % **Re-Ada(TPP)** were found to pass from the hybrid in suspension in water to a chloroform phase after 15 h of contact without stirring. After 24 h, the proportion of **Re-Phe(TPP)** in chloroform was 37 %, and it can be extrapolated that the amount of **Re-Ada(TPP)** is below this value, although it could not be determined accurately because of strong variation of the baseline. In summary, the **Re-Phe(TPP)/CNC** hybrid significantly releases complex molecules over time, while **Re-Ada(TPP)/CNC** is more stable, due to the lower solubility of the complex in water. However, it can be considered that in both cases, during the first two hours after dilution, which largely correspond to the incubation and irradiation time in the subsequent experiments in the presence of bacteria, a large proportion of the complex molecules is retained on the surface of the CNCs.

3.5. CO-photoproduction by hybrids in aqueous medium

The **Re-Phe(TPP)/CNC** and **Re-Ada(TPP)/CNC** hybrids considered for the photochemical study were prepared from 6.7×10^{-5} M and 4.0×10^{-5} M complexes, respectively, and CNCs at 1.6 mg/mL. In these conditions, the photoCORM/CNC ratio was well below the MAC value, and it can be assumed that all molecules of complexes were well dispersed at the CNC surface. Under irradiation at 350 nm, the UV–vis absorption spectra of the hybrids showed the same evolution as that observed for the free complexes (Fig. S33). Remarkably, the reaction was much slower, since it was only completed after 15 min. The phosphorescence was also extinguished after the photochemical process.

Qualitatively, it can be said that the photoreaction leads to the release of one CO molecule per complex molecule in the presence and in absence of CNCs. Thus, adsorption of the photoCORMs on CNCs does not prevent photochemical reactivity. In every case, the photodecarbonylation follows a kinetic law of order 1. For technical reasons, the photodecarbonylation quantum yield was not determined for the hybrids, but it is known that there is a direct link between photoreaction quantum yields and the initial slope of time-resolved absorbance profiles [85]. It can be concluded that photodecarbonylation is less efficient for

hybrids than for free complexes. This may be attributed to a slight variation of the energy levels of the adsorbed complex, which would make it more difficult to populate the dissociating, thermally-accessible metal-centered (MC) state, although no changes were observed by UV–vis absorption and emission spectroscopy for the other excited states. More likely, the approach of acetonitrile molecules and the ligand substitution may be uneasy for reasons of geometry or steric hindrance when the complex is adsorbed on the CNCs.

3.6. Photoproduction of singlet oxygen

The photoproduction of singlet oxygen ($^1O_2$) by complexes and hybrids was quantified *in situ* according to the indirect method of Kraljic and El Mohsni [78]. As its generation progresses, $^1O_2$ is captured by an imidazole derivative, resulting in the formation of a specific *trans*-annular peroxide intermediate, which then induces the bleaching of *p*-nitrosodimethylaniline (RNO). The absorbance variation of the mixture was then recorded at 440 nm as function of irradiation time. Remarkably, the curve exhibited a sharp rise during the first minutes, followed by a steady decrease over several hours (Fig. 6a). The ascending part of the curve can be attributed to the absorbance increase due to photodecarbonylation, which dominates the decrease due to bleaching of RNO. In this case, $^1O_2$ could be produced by both the photoCORM and D-photoCORM, in variable proportions as a function of time. After the first minutes, the decreasing curve reflects only the production of $^1O_2$ from the decarbonylated complexes. It was considered that the production of $^1O_2$ by the photoCORM plays a minor role in relation to the whole process, and so only the straight decreasing line was processed to access the $^1O_2$ photogeneration constants Φ_Δ. The comparison of the various systems showed that the photoproduction of $^1O_2$ is unexpectedly more efficient for **Re-Phe(TPP)** than for **Re-Ada(TPP)**. It remains quite efficient for the hybrids, although slightly weaker than for free complexes, which can be explained by the easiest access of dissolved dioxygen for the latter ones. If comparing our values with the literature data for other Re(I) photoCORMs in water, our free complexes generate less $^1O_2$ than some of the complexes incorporating trialkylphosphosphine ligands reported by Marker *et al.* [22].

From a general point of view, this photochemical study reveals the involvement of a remarkable two-step process, *i.e.* a fast photoproduction of CO by the native photoCORMs, followed by a prolonged photoproduction of $^1O_2$ by the decarbonylated complexes (Fig. 6b).

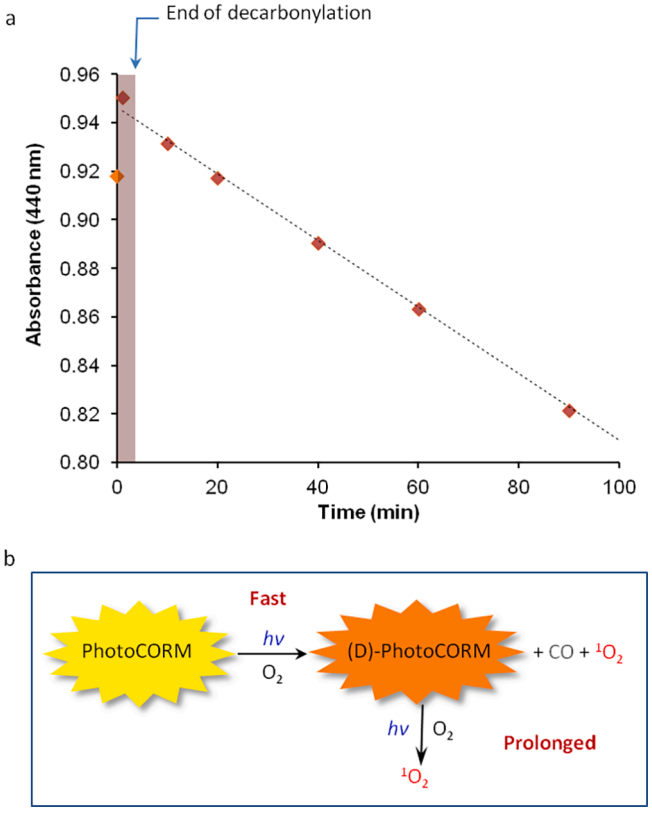

Fig. 6. A) Evolution of absorbance at 440 nm of a solution of complex **Re-Phe (TPP)** (1.1×10^{-5} M), *L*-histidine (1.0×10^{-2} M) and *p*-nitrosodimethylaniline (2.5×10^{-5} M) in water/acetonitrile 96:4 v/v, under irradiation at 350 nm. b) Schematized two-step photoproduction of active species by photoCORM and D-photoCORM.

3.7. Microbiological study

Finally, the antibacterial activity of the free photoCORMs and photoCORM/CNC hybrids against a Gram-positive strain, *i.e. Staphylococcus aureus*, and a Gram-negative strain, *Pseudomonas aeruginosa*, was investigated. The hybrids are the same as those used for the photochemical study, and the amount of complex molecules integrated into the hybrid can be directly compared to that of the free complexes. For the sake of comparison were also considered the free decarbonylated photoproduct **D-Re-Phe(TPP)**, generated by irradiation of **Re-Phe(TPP)** in acetonitrile for 15 min, as well as the synthesis precursors **Re-Phe(Cl)** and **Re-Ada(Cl)**. Bacteria were pre-incubated for 1 h in the presence of these compounds, irradiated at 365 nm, and incubated again for 24 h. A comparison was made with non-irradiated samples. Interestingly, when the suspensions of *S. aureus* pre-incubated with **Re-Phe(TPP)** or **Re-Ada (TPP)** were centrifuged, the pellets exhibited strong phosphorescence, showing that the free photoCORMs have an affinity for bacteria (Fig. 7a–c). This effect was not observed in the presence of **Re-Phe(Cl)**. For photoCORMs, the phosphorescence extinction also ensures that the photochemical reaction has taken place in the presence of bacteria (Fig. 7d,e). The values of the minimal inhibitory concentration (MIC), *i. e.* the lowest concentration of a compound at which bacterial growth is completely inhibited, were measured in the dark and after irradiation at 365 nm (Table 4). When the MIC values seemed interesting, the minimal bactericidal concentrations (MBC) that allows killing 99.9 % of bacteria, were also measured. In every case, the MBC values were very close to the MIC values, showing the bactericidal effect of the compounds.

The first striking result is that a strong bactericidal effect was observed for **Re-Phe(TPP)** against *S. aureus*, for which both MIC were as low as 2 $\mu g.mL^{-1}$. However, this effect was not correlated with photochemistry, it was even slightly weaker after irradiation, and so it can be attributed solely to direct biological toxicity. Regarding the hybrid **Re-Phe(TPP)/CNC**, there is a significant decrease in activity compared to the free complex, and still no photochemical effect. Possibly, the weak efficiency is due to the small amount of complex molecules that diffuse in the medium. This confirms that the antibacterial activity of complex

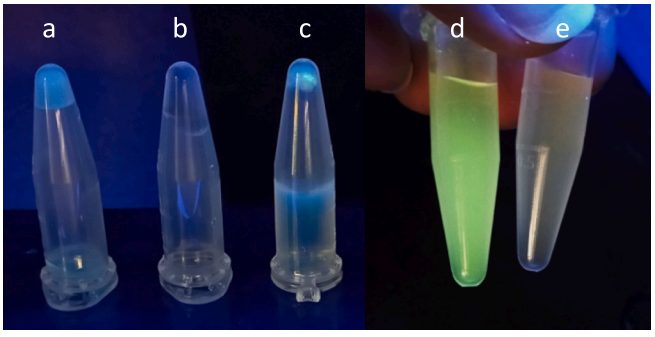

Fig. 7. Observation under illumination at 365 nm of the pellet of centrifuged samples of (a) *S. aureus*, (b) **Re-Ada(TPP)**, and (c) *S. aureus* with **Re-Ada(TPP)**, after removal of the supernatant. Sample of *S. aureus* with **Re-Ada(TPP)** before (d) and after 10 min irradiation at 365 nm (e). Samples in PBS after 1 h incubation at 37 °C. PhotoCORM concentration: 6.4×10^{-5} M.

Table 4
Minimal inhibitory concentration (MIC) (μM) of free complexes and hybrids towards two bacteria strains, with and without irradiation at 365 nm. Two references were used as controls: Methylene Blue dye (MB) and Gentamicin. In presence of MB, bacteria were irradiated or not with white light LED. All experiments were performed in triplicate.

Compound	*S. aureus*		*P. aeruginosa*	
	Light	**Dark**	**Light**	**Dark**
Re-Phe(TPP)	4	2	>125	>125
Re-Ada(TPP)	3	12	>125	>125
(D)-Re-Phe(TPP)	16	16	>125	>125
Re-Phe(Cl)	>125	>125	>125	>125
Re-Ada(Cl)	>125	>125	>125	>125
Re-Phe(TPP)/CNC	32	32	>125	>125
Re-Ada(TPP)/CNC	4	16	>125	>125
Methylene Blue	20	>125	40	>125
Gentamicin	2	2	4	4

Re-Phe(TPP) is linked to its mobility, and thus to its capacity to reach its biological target on which it exerts a toxic effect. In contrast, the free complex **Re-Ada(TPP)** was more active after irradiation than in the dark. This photochemical effect was also observed for hybrid **Re-Ada (TPP)/CNC**, although the activity of the latter was reduced with respect to that of the free complex. It can be thought that **Re-Ada(TPP)** cumulates the effect of CO (and/or $^1O_2$) and an intrinsic biological effect. A possibility is that CO enhances the permeation of the bacterial membrane, thus allowing the hydrophobic photoCORM to penetrate more easily inside the bacteria. Due to the presence of the adamantyl moiety, **Re-Ada(TPP)** may also have a biological target that is not that of **Re-Phe (TPP)**, and this could explain the different behavior of the two complexes despite a very similar photoreactivity. This observation underlines the value of the adamantyl group in drug design [55,56].

Besides, the decarbonylated photoproduct **D-Re-Phe(TPP)** induced weaker bacterial effect than the native photoCORM, suggesting that the former is less toxic towards bacteria and that the generation of $^1O_2$ alone is not enough to reverse this trend. The neutral complexes **Re-Phe(Cl)** and **Re-Ada(Cl)**, which are very weakly soluble in water, showed no effect at all, probably because they do not enter the bacteria. This hypothesis is comforted by the observation that none of our systems show antibacterial activity against *P. aeruginosa.* Indeed, Gram-negative bacteria have additional outer membrane, as well as an abundance of efflux pumps and highly selective porins, which make intracellular targets particularly difficult to reach [86]. It can be assumed that CO and $^1O_2$ diffuse passively through all bacterial membranes, but their concentration in our systems may not be sufficient to induce an antibacterial effect. Another possibility is that these species, and in particular CO, must be generated inside bacteria to be fully active, as has been suggested several times for CORMs in the literature [25,38].

4. Conclusions

The mechanisms by which photoCORMs act on bacteria are still poorly understood. They are apparently very complicated because they involve numerous biological targets, and depend on the nature of the photoCORMs and bacterial strains. The present work allowed the development of original tools for a better understanding of the processes involved. It appeared that **Re-Phe(TPP)** has strong bactericidal effect on *S. aureus*, mainly due to the intrinsic toxicity of this complex. This confirms that the effect of photoCORMs is more complicated than it seems. Indeed, the lack of significant CO-mediated effects has already been reported for some CORMs and photoCORMs [19,27]. It is also known that some of these compounds damage the bacteria membranes without photochemical activation, and this explains their effectiveness as conventional antibiotic adjuvants [41,42]. Two distinct modes of action, with and without photochemical activation, may also co-exist for the same compound [48]. In the present case, in-depth biological studies sustained by a docking approach [87] would be instructive to better understand the mode of action of **Re-Phe(TPP)** and possibly improve its chemical structure. Toxicity tests on eukaryotic cells will be necessary to say if this complex can be used in therapeutics. It was shown with **Re-Ada (TPP)** that the production of CO probably contributes to the efficiency of the complex, but at the moment, the synergistic effect (photoCORM + CO + $^1O_2$) is not as efficient as expected. To the best of our knowledge, this work reports the first example of hybrids formed between CNCs and photoCORMs. Although not very effective as such, these hybrids are stable, easy to handle in aqueous media and to incorporate in various formulations. As CNC platforms are quite versatile, they could be modified to allow a better diffusion of the photoCORM molecules in the medium. For example, the insertion of the rhenium complex can be mediated by a cyclodextrin provided with a positively-charged chain [76], which, according to our preliminary studies, makes the system much more dynamic. CNCs could also carry a photosensitizer better than Re(I) complexes, to reinforce the synergistic effect [88]. Lastly, the system can be improved by designing photoCORMs that absorb visible light in view of practical applications [32,73,74]. Consequently, this work opens new perspectives towards efficient bactericidal materials, potentially usable for fighting antibioresistant bacteria.

CRediT authorship contribution statement

Valentine Guilbaud: Writing – original draft, Methodology, Investigation. **Marie Goizet:** Writing – original draft, Investigation. **Nadine Leygue:** Writing – review & editing, Investigation. **Alexandre Poirot:** Writing – review & editing, Investigation. **Sonia Mallet-Ladeira:** Writing – review & editing, Investigation. **Charles-Louis Serpentini:** Writing – review & editing, Investigation. **Tan-Sothéa Ouk:** Writing – review & editing, Methodology. **Gauthier M.A. Ndong Ntoutoume:** Writing – review & editing, Methodology. **Vincent Sol:** Writing – review & editing, Supervision, Methodology, Funding acquisition. **Eric Benoist:** Writing – review & editing, Supervision, Project administration, Conceptualization. **Suzanne Fery-Forgues:** Writing – original draft, Methodology, Investigation, Funding acquisition, Conceptualization.

Declaration of competing interest

The authors declare that they have no known competing financial interests or personal relationships that could have appeared to influence the work reported in this paper.

Data availability

Data will be made available on request.

Acknowledgements

ANR is gratefully acknowledged for funding (PANTHERA project # ANR-22-CE29-0008). We thank Ms. Maëlle Deleuzière for performing TEM measurements. We are also extremely grateful to Mrs. Isabelle Fabing who kindly welcomed us into her laboratory, allowing us to complete our experiments in the best conditions.

Appendix A. Supplementary data

Supplementary data to this article can be found online at https://doi.org/10.1016/j.jphotochem.2024.115600.

References

[1] S.B. Zaman, M.A. Hussain, R. Nye, V. Mehta, K.T. Mamun, N. Hossain, A review on antibiotic resistance: Alarm bells are ringing, Cureus 9 (2017) e1403.
[2] X. Yang, W. Lu, C.P. Hopper, B. Kec, B. Wang, Nature's marvels endowed in gaseous molecules I: Carbon monoxide and its physiological and therapeutic roles

acta Pharm, Sinica B 11 (2021) 1434–1445, https://doi.org/10.1016/j.apsb.2020.10.010.
[3] J.L. Wilson, H.E. Jesse, R.K. Poole, K.S. Davidge, Antibacterial effects of carbon monoxide, Curr. Pharma. Biotechnol. 13 (2012) 760–768, https://doi.org/10.2174/138920112800399329.
[4] B.Y. Chin, L.E. Otterbein, Carbon monoxide is a poison to microbes! CO as a bactericidal molecule, Curr. Opin. Pharmacol. 9 (2009) 490–500, https://doi.org/10.1016/j.coph.2009.06.025.
[5] W.-C. Shen, X. Wang, W.-T. Qin, Y.F. Qiu, B.W. Sun, Exogenous carbon monoxide suppresses *Escherichia coli* vitality and improves survival in an *Escherichia coli*-induced murine sepsis model, Acta Pharmacol. Sinica 35 (2014) 1566–1576, https://doi.org/10.1038/aps.2014.99.
[6] H.-I. Choi, A. Zeb, M.-S. Kim, I. Rana, N. Khan, O.S. Qureshi, C.-W. Lim, J.-S. Park, Z. Gao, H.-J. Maeng, J.-K. Kim, Controlled therapeutic delivery of CO from carbon monoxide-releasing molecules (CORMs), J. Control. Release 350 (2022) 652–667, https://doi.org/10.1016/j.jconrel.2022.08.055.
[7] K. Ling, F. Men, W.-C. Wang, Y.-Q. Zhou, H.-W. Zhang, D.-W. Ye, Carbon monoxide and its controlled release: therapeutic application, detection, and development of Carbon monoxide releasing molecules (CORMs), J. Med. Chem. 61 (2018) 2611–2635, https://doi.org/10.1021/acs.jmedchem.6b01153.
[8] X.-X. Yang, B.-W. Ke, W. Lu, B.-H. Wang, CO as a therapeutic agent: discovery and delivery forms, Chin. J. Nat. Med. 18 (2020) 284–295, https://doi.org/10.1016/S1875-5364(20)30036-4.
[9] K. Koike, N. Okoshi, H. Hori, K. Takeuchi, O. Ishitani, H. Tsubaki, I.P. Clark, M. W. George, F.P.A. Johnson, J.J. Turner, Mechanism of the photochemical ligand substitution reactions of fac-[Re(bpy)(CO)3(PR3)]+ complexes and the properties of their triplet ligand-field excited states, J. Am. Chem. Soc. 124 (2002) 11448–11455, https://doi.org/10.1021/ja017032m.
[10] K. Saita, Y. Harabuchi, T. Taketsugu, O. Ishitani, S. Maeda, Theoretical study on mechanism of the photochemical ligand substitution of fac-[ReI(bpy)(CO)3(PR3)]+ complex, Phys. Chem. Chem. Phys. 18 (2016) 17557–17564, https://doi.org/10.1039/C6CP02314B.
[11] A.E. Pierri, A. Pallaoro, G. Wu, P.C. Ford, A luminescent and biocompatible PhotoCORM, J. Am. Chem. Soc. 134 (2012) 18197–18200, https://doi.org/10.1021/ja3084434. Corrigenda: J. Am. Chem. Soc. 134 (2012) 18197−18200. DOI: 10.1021/ja3084434.
[12] I. Chakraborty, S.J. Carrington, P.K. Mascharak, Design strategies to improve the sensitivity of photoactive metal carbonyl complexes (photoCORMs) to visible light and their potential as CO-donors to biological targets, Acc. Chem. Res. 47 (2014) 2603–2611, https://doi.org/10.1021/ar500172f.
[13] I. Chakraborty, J. Jimenez, W.M.C. Sameera, M. Kato, P.K. Mascharak, Luminescent Re(I) Carbonyl complexes as Trackable PhotoCORMs for CO delivery to Cellular Targets, Inorg. Chem. 56 (2017) 2863–2873, https://doi.org/10.1021/acs.inorgchem.6b02999.
[14] E. Kottelat, F. Zobi, Visible light-activated PhotoCORMs, Inorganics 5 (2017) 24, https://doi.org/10.3390/inorganics5020024.
[15] M.N. Pinto, P.K. Mascharak, Light-assisted and remote delivery of carbon monoxide to malignant cells and tissues, J. Photochem. Photobiol. C 42 (2020) 100341, https://doi.org/10.1016/j.jphotochemrev.2020.100341.
[16] J. Jimenez, I. Chakraborty, A. Dominguez, J. Martinez-Gonzalez, W.M.C. Sameera, P.K. Mascharak, A luminescent manganese PhotoCORM for CO delivery to Cellular Targets under the control of visible light, Inorg. Chem. 57 (2018) 1766–1773, https://doi.org/10.1021/acs.inorgchem.7b02480.
[17] T. Soboleva, L.M. Berreau, Tracking CO release in cells via the luminescence of donor molecules and/or their by-products, Isr. J. Chem. 59 (2019) 339–350, https://doi.org/10.1002/ijch.201800172.
[18] L.S. Lazarus, A.D. Benninghoff, L.M. Berreau, Development of triggerable, Trackable, and Targetable Carbon monoxide releasing molecules, Acc. Chem. Res. 53 (2020) 2273–2285, https://doi.org/10.1021/acs.accounts.0c00402.
[19] N. Bauer, Z. Yuan, X. Yang, B. Wang, Plight of CORMs: the unreliability of four commercially available CO-releasing molecules, CORM-2, CORM-3, CORM-A1, and CORM-401, in studying CO biology, Biochem. Pharmacol. 214 (2023) 115642, https://doi.org/10.1016/j.bcp.2023.115642.
[20] N. Abeyrathna, K. Washington, C. Bashurb, Y. Liao, Nonmetallic carbon monoxide releasing molecules (CORMs), Org. Biomol. Chem. 15 (2017) 8692–8699, https://doi.org/10.1039/C7OB01674C.
[21] K. Schindler, F. Zobi, Anticancer and antibiotic rhenium tri- and Dicarbonyl complexes: current Research and future perspectives, Molecules 27 (2022) 539, https://doi.org/10.3390/molecules27020539.
[22] S.C. Marker, S.N. MacMillan, W.R. Zipfel, Z. Li, P.C. Ford, J.J. Wilson, Photoactivated in vitro anticancer activity of Rhenium(I) Tricarbonyl complexes Bearing water-soluble phosphines, Inorg. Chem. 57 (2018) 1311–1331, https://doi.org/10.1021/acs.inorgchem.7b02747.
[23] A. Ismailova, D. Kuter, S. Bohle, I.S. Butler, An overview of the potential therapeutic applications of CO-releasing molecules, Bioinorg. Chem. Appl. 2018 (2018) 8547364, https://doi.org/10.1155/2018/8547364.
[24] L.S. Nobre, J.D. Seixas, C.C. Romão, L.M. Saraiva, Antimicrobial action of Carbon monoxide-releasing compounds, Antimicrob. Agents Chemother. 51 (2007) 4303–4307, https://doi.org/10.1128/AAC.00802-07.
[25] J.L. Wilson, H.E. Jesse, B.M. Hughes, V. Lund, K. Naylor, K.S. Davidge, G.M. Cook, B.E. Mann, R.K. Poole, Ru(CO)3Cl(glycinate) (CORM-3): a CO-releasing molecule with broad-spectrum antimicrobial and photosensitive activities against respiration and cation transport in Escherichia coli, Antioxid. Redox Signal. 19 (2013) 497–509, https://doi.org/10.1089/ars.2012.4784.
[26] K.S. Davidge, G. Sanguinetti, C.H. Yee, A.G. Cox, C.W. McLeod, C.E. Monk, B. E. Mann, R. Motterlini, R.K. Poole, Carbon monoxide-releasing antibacterial molecules Target respiration and global transcriptional regulators, J. Biol. Chem. 284 (2009) 4516–4524, https://doi.org/10.1074/jbc.M808210200.
[27] H.M. Southam, M.P. Williamson, J.A. Chapman, R.L. Lyon, C.R. Trevitt, P.J. F. Henderson, R.K. Poole, 'Carbon-monoxide-releasing Molecule-2 (CORM-2)' is a Misnomer: ruthenium toxicity, not CO release, accounts for its antimicrobial effects, Antioxidants 10 (2021) 915, https://doi.org/10.3390/antiox10060915.
[28] Z. Yuan, X. Yang, Y. Ye, R. Tripathi, B. Wang, Chemical reactivities of two widely used ruthenium-based CO-releasing molecules with a range of biologically important reagents and molecules, Anal. Chem. 93 (2021) 5317–5326, https://doi.org/10.1021/acs.analchem.1c00533.
[29] S. McLean, R. Begg, H.E. Jesse, B.E. Mann, G. Sanguinetti, R.K. Poole, Analysis of the bacterial response to Ru(CO)3Cl(Glycinate) (CORM-3) and the inactivated compound identifies the role played by the ruthenium compound and reveals sulfur-containing species as a major Target of CORM-3 action, Antioxid. Redox Signal. 19 (2013) 1999–2012, https://doi.org/10.1089/ars.2012.5103.
[30] L.K. Wareham, R. Begg, H.E. Jesse, J.W.A. van Beilen, S. Ali, D. Svistunenko, S. McLean, K.J. Hellingwerf, G. Sanguinetti, R.K. Poole, Carbon monoxide gas is not inert, but global, in its consequences for bacterial gene expression, iron acquisition, and antibiotic resistance, Antioxid. Redox Signal. 24 (2016) 1013–1028, https://doi.org/10.1089/ars.2015.6501.
[31] M. Patra, M. Wenzel, P. Prochnow, V. Pierroz, G. Gasser, J.E. Bandow, N. Metzler-Nolte, An organometallic structure-activity relationship study reveals the essential role of a Re(CO)3 moiety in the activity against gram-positive pathogens including MRSA, Chem. Sci. 6 (2015) 214–224, https://doi.org/10.1039/c4sc02709d.
[32] K. Schindler, Y. Cortat, M. Nedyalkova, A. Crochet, M. Lattuada, A. Pavic, F. Zobi, Antimicrobial activity of rhenium di- and Tricarbonyl diimine complexes: insights on membrane-Bound S. aureus protein binding, Pharmaceuticals 15 (2020) 1107, https://doi.org/10.3390/ph15091107.
[33] S.M. Carvalho, J. Marques, C.C. Romão, L.M. Saraiva, Metabolomics of Escherichia coli treated with the antimicrobial Carbon monoxide-releasing molecule CORM-3 reveals Tricarboxylic acid cycle as major Target, Antimicrob. Agents Chemother. 63 (2019) e00643–e00719, https://doi.org/10.1128/AAC.00643-19.
[34] J.L. Wilson, L.K. Wareham, S. McLean, R. Begg, S. Greaves, B.E. Mann, G. Sanguinetti, R.K. Poole, CO-releasing molecules have nonheme Targets in bacteria: transcriptomic, mathematical modeling and biochemical analyses of CORM-3 [Ru(CO)3Cl(glycinate)] actions on a heme-deficient mutant of Escherichia coli, Antioxid. Redox Signal. 23 (2015) 148–162, https://doi.org/10.1089/ars.2014.6151.
[35] M. Desmard, R. Foresti, D. Morin, M. Dagouassat, A. Berdeaux, E. Denamur, S. H. Crook, B.E. Mann, D. Scapens, P. Montravers, J. Boczkowski, R. Motterlini, Differential antibacterial activity against *Pseudomonas aeruginosa* by Carbon monoxide-releasing molecules, Antioxid. Redox Signal. 16 (2011) 153–163, https://doi.org/10.1089/ars.2011.3959.
[36] J. Cheng, J. Hu, Recent advances on Carbon monoxide releasing molecules for antibacterial applications, ChemMedChem 16 (2021) 3628–3634, https://doi.org/10.1002/cmdc.202100555.
[37] L.K. Wareham, R.K. Poole, M. Tinajero-Trejo, CO-releasing metal Carbonyl compounds as antimicrobial agents in the post-antibiotic era, J. Biol. Chem. 290 (2015) 18999–19007, https://doi.org/10.1074/jbc.r115.642926.
[38] L.S. Nobre, H. Jeremias, C.C. Romão, L.M. Saraiva, Examining the antimicrobial activity and toxicity to animal cells of different types of CO-releasing molecules, Dalton Trans. 45 (2016) 1455–1466, https://doi.org/10.1039/c5dt02238j.
[39] A.F.N. Tavares, M. Teixeira, C.C. Romão, J.D. Seixas, L.S. Nobre, L.M. Saraiva, Reactive oxygen species mediate bactericidal killing elicited by Carbon monoxide-releasing molecules, J. Biol. Chem. 286 (2011) 26708, https://doi.org/10.1074/jbc.M111.255752.
[40] A. Liakopoulos, R.M. La Ragione, C. Nagel, U. Schatzschneider, D.E. Rozen, J. W. Betts, Manganese complex [Mn(CO)3(tpa-k3N)]Br increases antibiotic sensitivity in multidrug-resistant Streptococcus pneumonia, J. Glob. Antimicrob. Resist. 22 (2020) 594–597, https://doi.org/10.1016/j.jgar.2020.04.031.
[41] N. Rana, H. E. Jesse, M. Tinajero-Trejo, J. A. Butler, J. D. Tarlit, M. L. von und zur Muhlen, C. Nagel, U. Schatzschneider, R. K. Poole, A manganese photosensitive tricarbonyl molecule [Mn(CO)$_3$(tpak^{3}N)]Br enhances antibiotic efficacy in a multi-drug-resistant *Escherichia coli*, Microbiology, 163 (2017) 1477–1489. DOI 10.1099/mic.0.000526.
[42] S.S. Mendes, J. Marques, E. Mesterházy, J. Straetener, M. Arts, T. Pissarro, J. Reginold, A. Berscheid, J. Bornikoel, R.M. Kluj, C. Mayer, F. Oesterhelt, S. Friães, B. Royo, T. Schneider, H. Brötz-Oesterhelt, C.C. Romão, L.M. Saraiva, Synergetic antimicrobial activity and mechanism of clotrimazole-linked CO-releasing molecules, ACS Bio. Med. Chem. Au 2 (2022) 419–436, https://doi.org/10.1021/acsbiomedchemau.2c00007.
[43] A.F. Tavares, M.R. Parente, M.C. Justino, M. Oleastro, L.S. Nobre, L.M. Saraiva, The bactericidal activity of Carbon monoxide-releasing molecules against Helicobacter pylori, PLoS ONE 8 (2013) e83157.
[44] M. Tinajero-Trejo, N. Rana, C. Nagel, H.E. Jesse, T.W. Smith, L.K. Wareham, M. Hippler, U. Schatzschneider, R.K. Poole, Antimicrobial activity of the manganese photoactivated Carbon monoxide-releasing molecule [Mn(CO)3(tpa-j3N)]+ against a pathogenic Escherichia coli that causes Urinary infections, Antioxid. Redox Signal. 24 (2016) 765–780, https://doi.org/10.1089/ars.2015.6484.
[45] S. McMahon, A. Rajagopal, S. Amirjalayer, Y. Halpin, D. Fitzgerald-Hughes, W. J. Buma, S. Woutersen, C. Long, M.T. Pryce, Photo-activated CO-release in the amino tungsten fischer carbene complex, [(CO)5WC(NC4H8)Me], picosecond time resolved infrared spectroscopy, time-dependent density functional theory, and an antimicrobial study, J. Inorg. Biochem. 208 (2020) 111071, https://doi.org/10.1016/j.jinorgbio.2020.111071.

[46] A. Toscani, C. Hind, M. Clifford, S.-H. Kim, A. Gucic, C. Woolley, N. Saeed, K. M. Rahman, J.M. Sutton, D. Castagnolo, Development of photoactivable phenanthroline-based manganese(I) CO-releasing molecules (PhotoCORMs) active against ESKAPE bacteria and bacterial biofilms, Eur. J. Med. Chem. 213 (2021) 113172, https://doi.org/10.1016/j.ejmech.2021.113172.
[47] J.S. Ward, J.M. Lynam, J. Moir, I.J.S. Fairlamb, Visible-light-induced CO release from a therapeutically viable tryptophan-derived Manganese(I) Carbonyl (TryptoCORM) exhibiting potent inhibition against E. coli, Chem. Eur. J. 20 (2014) 15061–15068, https://doi.org/10.1002/chem.201403305.
[48] A. Frei, M. Amado, M.A. Cooper, M.A.T. Blaskovich, Light-activated rhenium complexes with dual mode of action against bacteria, Chem. Eur. J. 26 (2020) 2852–2858, https://doi.org/10.1002/chem.201904689.
[49] A.C. Kautz, P.C. Kunz, C. Janiak, CO-releasing molecule (CORM) conjugate systems, Dalton Trans. 45 (2016) 18045–18063, https://doi.org/10.1039/c6dt03515a.
[50] H. Yan, J. Du, S. Zhu, G. Nie, H. Zhang, Z. Gu, Y. Zhao, Emerging delivery strategies of Carbon monoxide for therapeutic applications: from CO gas to CO releasing nanomaterials, Small 15 (2019) 1904382, https://doi.org/10.1002/smll.201904382.
[51] D. Nguyen, T.-K. Nguyen, S.A. Rice, C. Boyer, CO-releasing Polymers exert antimicrobial activity, Biomacromolecules 16 (2015) 2776–2786, https://doi.org/10.1021/acs.biomac.5b00716.
[52] M. Klinger-Strobel, S. Gläser, O. Makarewicz, R. Wyrwa, J. Weisser, M.W. Pletz, A. Schiller, Bactericidal effect of a photoresponsive carbon monoxide releasing nonwoven against Staphylococcus aureus biofilms, Antimicrob. Agents Chemother. 60 (2016) 4037–4046, https://doi.org/10.1128/AAC.00703-16.
[53] Á.D. Hernández Mejías, A. Poirot, M. Rmili, N. Leygue, M. Wolff, N. Saffon-Merceron, E. Benoist, S. Fery-Forgues, Efficient photorelease of carbon monoxide from a luminescent tricarbonyl rhenium(I) complex incorporating pyridyl-1,2,4-triazole and phosphine ligands, Dalton Trans. 50 (2021) 1313–1323, https://doi.org/10.1039/D0DT03577G.
[54] A. Poirot, C. Vanucci-Bacqué, B. Delavaux-Nicot, N. Leygue, N. Saffon-Merceron, F. Alary, F. Bedos-Belval, E. Benoist, S. Fery-Forgues, Phenyl-1,2,4-pyta-tricarbonylrhenium(I) complexes: combining a simplified structure and steric hindrance to modulate the photoluminescence properties, Dalton Trans. 50 (2021) 13686–13698, https://doi.org/10.1039/D1DT02161C.
[55] J. Liu, D. Obando, V. Liao, T. Lifa, R. Codd, The many faces of the adamantyl group in drug design, Eur. J. Med. Chem. 46 (2011) 1949–1963, https://doi.org/10.1016/j.ejmech.2011.01.047.
[56] K. Spilovska, F. Zemek, J. Korabecny, E. Nepovimova, O. Soukup, M. Windisch, K. Kuca, Adamantane – a lead structure for drugs in clinical practice, Curr. Med. Chem. 23 (2016) 3245–3266, https://doi.org/10.2174/0929867323666160525114026.
[57] P. Mali, A.P. Sherje, Cellulose nanocrystals: fundamentals and biomedical applications, Carbohydr. Polym. 275 (2022) 118668, https://doi.org/10.1016/j.carbpol.2021.118668.
[58] J. Shojaeiarani, D. Bajwa, A. Shirzadifar, A review on cellulose nanocrystals as promising biocompounds for the synthesis of nanocomposite hydrogels, Carbohydr. Polym. 216 (2019) 47–269, https://doi.org/10.1016/j.carbpol.2019.04.033.
[59] F. Le Guern, T.S. Ouk, K. Grenier, N. Joly, V. Lequart, V. Sol, Enhancement of photobactericidal activity of chlorin-e6-cellulose nanocrystals by covalent attachment of polymyxin B, Bioconj. Chem. 9 (2017) 2493–2506, https://doi.org/10.1039/C7TB01274H.
[60] M.N.F. Norrrahim, N.M. Nurazzi, M.A. Jenol, M.A.A. Farid, N. Janudin, F.A. Ujang, T.A.T. Yasim-Anuar, S.U.F.S. Najmuddin, R.A. Ilyas, Emerging development of nanocellulose as an antimicrobial material: an overview, Mater. Adv. 2 (2021) 3538–3551, https://doi.org/10.1039/D1MA00116G.
[61] A. Gülsu, E. Yüksektepe, Preparation of gentamicin conjugated cellulose nanocrystals and evaluation of efficacy on different microorganisms, Eur. J. Sci. Technol. 27 (2021) 1105–1112, https://doi.org/10.31590/ejosat.956593.
[62] V.T. Noronha, C.H.M. Camargos, J.C. Jackson, A.G. Souza Filho, A.J. Paula, C. A. Rezende, A.F. Faria, Physical membrane-stress-mediated antimicrobial properties of cellulose nanocrystals, ACS Sustain Chem. Eng. 9 (2021) 3203–3212, https://doi.org/10.1021/acssuschemeng.0c08317.
[63] SADABS, Program for data correction, Bruker-AXS.
[64] G.M. Sheldrick, SHELXT-integrated space-group and crystal-structure determination, Acta Cryst. A 71 (2015) 3–8, https://doi.org/10.1107/S2053273314026370.
[65] G.M. Sheldrick, Crystal structure refinement with SHELXL, Acta Cryst. C 71 (2015) 3–8, https://doi.org/10.1107/S2053229614024218.
[66] A.-R. Allouche, Gabedit—A graphical user interface for computational chemistry softwares, J. Comput. Chem. 32 (2011) 174–182, https://doi.org/10.1002/jcc.21600.
[67] C. Adamo, V. Barone, Toward reliable density functional methods without adjustable parameters: the PBE0 model, J. Chem. Phys. 110 (1999) 6158–6170, https://doi.org/10.1063/1.478522.
[68] J.P. Perdew, K. Burke, M. Ernzerhof, Generalized gradient approximation made simple, Phys. Rev. Lett. 77 (1996) 3865–3868, https://doi.org/10.1103/PhysRevLett.77.3865.
[69] P.J. Hay, W.R. Wadt, *Ab initio* effective core potentials for molecular calculations. Potentials for the transition metal atoms Sc to Hg, J. Chem. Phys. 82 (1985) 270–283, https://doi.org/10.1063/1.448799.
[70] P.J. Hay, W.R. Wadt, *Ab initio* effective core potentials for molecular calculations. Potentials for K to Au including the outermost core orbitals, J. Chem. Phys. 82 (1985) 299–310, https://doi.org/10.1063/1.448975.
[71] B. Mennucci, J. Tomasi, Continuum solvation models: a new approach to the problem of solute's charge distribution and cavity boundaries, J. Chem. Phys. 106 (1997) 5151, https://doi.org/10.1063/1.473558.
[72] M. Cossi, V. Barone, B. Mennucci, J. Tomasi, *Ab initio* study of ionic solutions by a polarizable continuum dielectric model, Chem. Phys. Lett. 286 (1998) 253–260, https://doi.org/10.1016/S0009-2614(98)00106-7.
[73] T. Lu, F. Chen, Multiwfn: a multifunctional wavefunction analyzer, J. Comput. Chem. 33 (2012) 580–592, https://doi.org/10.1002/jcc.22885.
[74] T. Lu, F. Chen, Calculation of molecular orbital composition, Acta Chim. Sinica 69 (2011) 2393–2406. http://sioc-journal.cn/Jwk_hxxb/CN/abstract/abstract340458.shtml.
[75] K. Suzuki, A. Kobayashi, S. Kaneko, K. Takehira, T. Yoshihara, H. Ishida, Y. Shiina, S. Oishi, S. Tobita, Reevaluation of absolute luminescence quantum yields of standard solutions using a spectrometer with an integrating sphere and a back-thinned CCD detector, Phys. Chem. Chem. Phys. 11 (2009) 9850–9860, https://doi.org/10.1039/B912178A.
[76] G.-M.-A. Ndong Ntoutoume, R. Granet, J.P. Mbakidi, F. Brégier, D.Y. Léger, C. Fidanzi-Dugas, V. Lequart, N. Joly, B. Liagre, V. Chaleix, V. Sol, Development of curcumin-cyclodextrin/cellulose nanocrystals complexes: new anticancer drug delivery systems, Bioorg. Med. Chem. Lett. 26 (2016) 941–945, https://doi.org/10.1016/j.bmcl.2015.12.060.
[77] C.G. Hatchard, C.A. Parker, A new sensitive chemical actinometer II. potassium ferrioxalate as a standard chemical actinometer, Proc. r. Soc. A 235 (1956) 518–536, https://doi.org/10.1098/rspa.1956.0102.
[78] I. Kraljić, S. El Mohsni, A new method for the detection of singlet oxygen in aqueous solutions, Photochem. Photobiol. 28 (1978) 577–581, https://doi.org/10.1111/j.1751-1097.1978.tb06972.x.
[79] M. DeRosa, R.J. Crutchley, Photosensitized singlet oxygen and its applications, Coord. Chem. Rev. 233–234 (2002) 351–371, https://doi.org/10.1016/S0010-8545(02)00034-6.
[80] A. Poirot, C. Vanucci-Bacqué, B. Delavaux-Nicot, C. Meslien, N. Saffon-Merceron, C.-L. Serpentini, F. Bedos-Belval, E. Benoist, S. Fery-Forgues, Using a diphenyl-bi-(1,2,4-triazole) tricarbonylrhenium(I) complex with intramolecular π–π stacking interaction for efficient solid-state luminescence enhancement, Dalton Trans. 52 (2023) 5453–5465, https://doi.org/10.1039/D2DT03573A.
[81] H. Tsubaki, S. Tohyama, K. Koike, H. Saitoh, O. Ishitani, Effect of intramolecular π–π and CH–π interactions between ligands on structure, electrochemical and spectroscopic properties of fac-[Re(bpy) (CO)3(PR3)]+ (bpy = 2,2′-bipyridine; PR3 = trialkyl or triarylphosphines), Dalton Trans. (2005) 385–395, https://doi.org/10.1039/B407947G.
[82] H. Tsubaki, A. Sekine, Y. Ohashi, K. Koike, H. Takeda, O. Ishitani, Control of photochemical, photophysical, electrochemical, and photocatalytic properties of Rhenium(I) complexes using Intramolecular weak Interactions between ligands, J. Am. Chem. Soc. 127 (2005) 15544–15555, https://doi.org/10.1021/ja053814u.
[83] C. Franco, J. Olmsted III, Photochemical determination of the solubility of oxygen in various media, Talanta 37 (1990) 905–909, https://doi.org/10.1016/0039-9140(90)80251-A.
[84] R. Díaz-Torres, S. Alvarez, Coordinating ability of anions and solvents towards transition metals and lanthanides, Dalton Trans. 40 (2011) 10742–10750, https://doi.org/10.1039/c1dt11000d.
[85] E. Stadler, A. Eibel, D. Fast, H. Freißmuth, K. Holly, M. Wiech, N. Moszner, G. Gescheidt, A versatile method for the determination of photochemical quantum yields via online UV-vis spectroscopy, Photochem. Photobiol. Sci. 17 (2018) 660–669, https://doi.org/10.1039/C7PP00401J.
[86] K.P. Romano, D.T. Hung, Targeting LPS biosynthesis and transport in gram-negative bacteria in the era of multi-drug resistance, Biochim. Biophys. Acta Mol. Cell. Res. 1870 (2023) 119407, https://doi.org/10.1016/j.bbamcr.2022.119407.
[87] M. Kaur Diksha, Reenu Megha, H. Kaur, V. Yempally, Rhenium (I) tricarbonyl complex with thiosemicarbazone ligand derived from Indole-2-carboxaldehyde: Synthesis, crystal structure, computational investigations, antimicrobial activity, and molecular docking studies, J. Mol. Struct. 1301 (2024) 137319, https://doi.org/10.1016/j.molstruc.2023.137319.
[88] W. Ma, X. Chen, L. Fu, J. Zhu, M. Fan, J. Chen, C. Yang, G. Yang, L. Wu, G. Mao, X. Yang, X. Mou, Z. Gu, X. Cai, Ultra-efficient antibacterial system based on photodynamic therapy and CO gas therapy for synergistic antibacterial and ablation biofilms, ACS Appl. Mater. Interfaces 12 (2020) 22479–22491, https://doi.org/10.1021/acsami.0c01967.